CORONAVIRUS

Viruses harness YxxØ motif to interact with host AP2M1 for replication: A vulnerable broad-spectrum antiviral target

Shuofeng Yuan[1,2,3,4], Hin Chu[1,2,3,4], Jingjing Huang[2], Xiaoyu Zhao[2], Zi-Wei Ye[2], Pok-Man Lai[2], Lei Wen[2], Jian-Piao Cai[2], Yufei Mo[5], Jianli Cao[2], Ronghui Liang[2], Vincent Kwok-Man Poon[2], Kong-Hung Sze[1,2,3], Jie Zhou[1,2,3,4], Kelvin Kai-Wang To[1,2,3,4,5], Zhiwei Chen[1,2,3,6], Honglin Chen[1,2,3,4], Dong-Yan Jin[7], Jasper Fuk-Woo Chan[1,2,3,4,5,8,*†], Kwok-Yung Yuen[1,2,3,4,5,8,*†]

Targeting a universal host protein exploited by most viruses would be a game-changing strategy that offers broad-spectrum solution and rapid pandemic control including the current COVID-19. Here, we found a common YxxØ-motif of multiple viruses that exploits host AP2M1 for intracellular trafficking. A library chemical, *N*-(p-amylcinnamoyl)anthranilic acid (ACA), was identified to interrupt AP2M1-virus interaction and exhibit potent antiviral efficacy against a number of viruses in vitro and in vivo, including the influenza A viruses (IAVs), Zika virus (ZIKV), human immunodeficiency virus, and coronaviruses including MERS-CoV and SARS-CoV-2. YxxØ mutation, AP2M1 depletion, or disruption by ACA causes incorrect localization of viral proteins, which is exemplified by the failure of nuclear import of IAV nucleoprotein and diminished endoplasmic reticulum localization of ZIKV-NS3 and enterovirus-A71-2C proteins, thereby suppressing viral replication. Our study reveals an evolutionarily conserved mechanism of protein-protein interaction between host and virus that can serve as a broad-spectrum antiviral target.

INTRODUCTION

Virus-host interactions drive mutual evolutionary changes which result in the marked diversification of viruses and host antiviral responses (*1*). The emergence of viruses including coronaviruses [Severe acute respiratory syndrome coronavirus (SARS-CoV), Middle East respiratory syndrome-related coronavirus (MERS-CoV), and Severe acute respiratory syndrome coronavirus 2 (SARS-CoV-2)], HIV, Zika virus (ZIKV), avian influenza A (H5N1), A (H7N9), and pandemic 2009 influenza A (pdmH1N1) viruses and enteroviruses [enterovirus A71 (EV-A71) and EV-D68] emphasizes the need to investigate for a conserved and broadly shared mechanism of virus-host interaction with potential therapeutic implications (*1*–*4*).

Viruses live briefly but perpetually. They invade cells and manipulate host machinery to replicate, transmit, and cause disease. Host signal transduction in response to virus invasion activates transcription factors that determine the gene expression characteristics and signaling mechanisms of the cell fate. These signaling mechanisms have been well studied in the fields of embryonic development and cancer biology but less well studied in the context of virus infection (*5*). A small set of evolutionarily conserved signaling pathways is associated with the cell fates of apoptosis, differentiation, or virus elimination during virus-host interactions. They include the transforming growth factor–β (TGF-β)/SMAD, Wnt/β-catenin, Notch, and phosphatidylinositol 3-kinase/thymoma viral proto-oncogene (PI3K/AKT) signaling pathways. Here, we show that TGF-β signaling is commonly altered by vastly different viruses. Modulating the TGF-β pathway is primarily mediated by mislocalization of TGF-β cytokines, its receptors TGF-βR, and SMAD transcriptional factors, which are largely executed through membrane and intracellular trafficking pathways (*6*). Therefore, we hypothesize that one approach to determine the cell fate, to die or to support virus replication, is through virus-manipulated membrane and intracellular trafficking. In this study, we performed integrative chemical and genetic screens that identified host AP2M1 protein as a critical player affecting TGF-β signaling and facilitating intracellular trafficking of different viruses. AP2M1 is the mu (μ2) subunit of AP2 adaptor complex, which functions as the major heterotetramer (α, β2, μ2, and σ2 subunits) that orchestrate clathrin-mediated endocytosis (CME) (*7*). The direct binding between TGF-βR and AP2 has been demonstrated in vitro and in vivo (*8*). Functionally, AP2M1 recognizes the YxxØ sorting motifs present in the cytosolic tail of different cargo proteins, whereas x refers to any amino acid and Ø indicates hydrophobic residues including L/M/F/I/V (*9*).

Here, we identify a previously unrecognized role of AP2M1, which is an intracellular cargo molecule that cotraffics with different internal viral proteins for proper subcellular localizations, in addition to its role in endocytosis. The cotrafficking is mediated through protein-protein interaction (PPI) between host AP2M1 and specific viral proteins harboring a YxxØ motif. Our initial pharmacological screening identifies a tool compound, *N*-(p-amylcinnamoyl)anthranilic acid (ACA), that disrupts AP2M1/YxxØ interaction without affecting

[1]State Key Laboratory of Emerging Infectious Diseases, Li Ka Shing Faculty of Medicine, The University of Hong Kong, Pokfulam, Hong Kong Special Administrative Region, China. [2]Department of Microbiology, Li Ka Shing Faculty of Medicine, The University of Hong Kong, Pokfulam, Hong Kong Special Administrative Region, China. [3]Carol Yu Centre for Infection, Li Ka Shing Faculty of Medicine, The University of Hong Kong, Pokfulam, Hong Kong Special Administrative Region, China. [4]Department of Clinical Microbiology and Infection Control, The University of Hong Kong-Shenzhen Hospital, Shenzhen, China. [5]Department of Microbiology, Queen Mary Hospital, Pokfulam, Hong Kong Special Administrative Region, China. [6]AIDS Institute, Li Ka Shing Faculty of Medicine, The University of Hong Kong, Hong Kong Special Administrative Region, China. [7]School of Biomedical Sciences, Li Ka Shing Faculty of Medicine, The University of Hong Kong, Pokfulam, Hong Kong Special Administrative Region, China. [8]Hainan Medical University-The University of Hong Kong Joint Laboratory of Tropical Infectious Diseases, Hainan Medical University, Haikou, Hainan, China.
*Corresponding author. Email: kyyuen@hku.hk (K.-Y.Y.); jfwchan@hku.hk (J.F.-W.C.)
†These authors contributed equally to this work.

the AP2M1 phosphorylation. ACA exhibits broad-spectrum antiviral efficacy in cell cultures and mouse models. Substitutions made in the influenza A nucleoprotein YxxØ motifs affect viral fitness in vitro and in vitro, indicating a critical role of AP2M1/YxxØ interaction during virus life cycle. Our study reveals AP2M1/YxxØ-mediated intracellular trafficking of diverse virus families, which represents a previously unidentified intervention target for a broad spectrum of emerging viral diseases.

RESULTS

TGF-β signaling is commonly altered upon virus infection

To determine the virus-induced signaling associated with cell fate pathways, we examined whether virus infection could potentiate host cell signaling by TGF-β, Wnt, Notch, and PI3K/Akt pathways. Reporter gene assays with high multiplicity of infection (MOI) and time-course monitoring of luciferase activity were performed in gene-transfected human primary cells including the influenza A pdmH1N1–infected human primary bronchial/tracheal epithelial cells (HBTECs), ZIKV-infected human primary fibroblasts HFL1 and EV-A71–infected human neural progenitor cells. TGF-β signaling exhibited distinct patterns of marked changes when compared with the marginally changed Wnt, Notch, and PI3K/Akt pathways (Fig. 1A). Infection by either pdmH1N1 or ZIKV triggered TGF-β activation, whereas EV-A71 infection suppressed its signaling, indicating that TGF-β signaling is commonly exploited in the cell fate determination pathway by different RNA viruses.

TGF-β–modulating membrane and intracellular trafficking is vulnerable to antiviral intervention

Proper control of TGF-βR via membrane and intracellular trafficking is documented to mediate TGF-β signaling (*10*). To explore the dependence of viral fitness on these host trafficking genes, we performed a loss-of-function screen to determine the degree of pdmH1N1 replication after individual gene silencing. Among the 142 cellular trafficking genes, knockdown of 17 genes reduced virus titers by more than one-$\log_{10}$ unit (Fig. 1B and fig. S1). Of the 17 influenza A virus (IAV) screen hits, 4 had been previously implicated in HIV-1 assembly, release, and budding: Adaptor related protein complex 1 subunit mu 1 (AP1M1), Caveolin 1 (CAV1), Ras-related protein Rab-5A (RAB5A), and Rho-associated protein kinase 1 (RCOK1) (*11*); depletion of COPA or COPB2 profoundly restricted human cytomegalovirus replication (*12*); COPG and AP2M1 were demonstrated to be important for IAV production in a genome-wide small interfering RNA (siRNA) screening (*13*). The results suggested that the selected membrane trafficking genes may serve as proviral factors with broad relevance to a number of virus infections. In view of the vulnerability of intracellular trafficking within virus life cycle, we screened a small-molecule compound library of trafficking inhibitors for finding drug hits with promising antiviral potency, which may also serve as a tool compound enabling the identification and characterization of putative targets within intracellular trafficking pathways. The library consists of 420 inhibitors targeting membrane transporters such as P-glycoprotein, Exportin 1, and ion channels including cystic fibrosis transmembrane conductance regulator, proton pump, calcium pump, etc. Multiple rounds of selection were performed using cell protection (supplementary data sheet) and viral load reduction assays, which identified 20 hits that suppressed virus replication for >3 logs at 10 μM and another 5 candidates achieving >2 logs inhibition at 1 μM (table S1). To prioritize these five compounds, we evaluated their antiviral efficacy against other emerging viruses and identified ACA as the only inhibitor that exhibited a broad-spectrum antiviral effect against influenza A H1N1, ZIKV, HIV-1, SARS-CoV-2, EV-A71, human adenovirus 5 (AdV5), and severe fever with thrombocytopenia syndrome virus (SFTSV) (Fig. 1C and fig. S2A).

The tool compound ACA is a broad-spectrum antiviral in vitro, ex vivo, and in vivo

The 50% cytotoxic concentration of ACA ranged from 20 to 120 μM in different cell lines, while its half maximal effective concentration (EC_{50}) was at or below micromolar levels (fig. S2A). ACA (10 μM) potently suppressed SARS-CoV-2 replication for >2 logs in both supernatants and cell lysates in Caco2 cells (EC_{50} = 0.59 μM), indicating a good therapeutic potential for the current COVID-19 pandemic (fig. S2B). Because ACA displayed the highest selectivity index of 219 against pdmH1N1 infection, ACA was tested against different IAV subtypes in the subsequent antiviral evaluations. Flow cytometry showed that the percentage of pdmH1N1-infected Madin-Darby canine kidney (MDCK) cells after 10 μM ACA treatment decreased by 83.2% at 24 hours post-infection (hpi) (Fig. 2A). ACA exhibited cross-protection against H5N1, H7N7, H7N9, and H9N2 in a dose-dependent manner (Fig. 2B). Notably, ACA treatment reduced supernatant viral titer by >4 logs HBTECs (Fig. 2C). Using our previously established proximal differentiated three-dimensional (3D) human airway organoids (AOs) for predicting the infectivity of influenza viruses in humans (*14*), we confirmed that ACA reduced virus replication by >4 logs (Fig. 2D), with markedly decreased expression of viral nucleoprotein (NP) antigen (Fig. 2E). Collectively, ACA robustly inhibited IAVs replication in vitro and ex vivo.

To determine ACA's toxicity, we intraperitoneally inoculated the maximal phosphate-buffered saline (PBS)–soluble ACA (6.75 mg/kg) into BALB/c mice for 10 days. No body weight loss or decreased activity was observed for a consecutive monitoring of 14 and 28 days, respectively (fig. S2C). To evaluate the in vivo antiviral protection of ACA, we challenged mice with 1000 plaque-forming units (PFU) of mouse-adapted H1N1 virus. All mice after a single intranasal (i.n.) dose of ACA (0.2 mg/kg) survived (n = 8), whereas all dimethyl sulfoxide (DMSO)–treated and zanamivir-treated (2 mg/kg) mice died (Fig. 2F). Using the same experimental regimen, ACA conferred substantial better survival against avian IAV H7N9 (100% versus 0%; Fig. 2F), notably less body weight loss (Fig. 2G), and undetectable lung tissue virus titers at days 2 and 4 after challenge (Fig. 2H). On 4 days post-infection (dpi), histopathologic examination showed substantially less pulmonary alveolar damage and interstitial inflammatory infiltration in ACA-treated mice (Fig. 2I). Together, ACA effectively protected mice challenged by two IAV subtypes by reducing virus replication and pneumonia.

The broad-spectrum antiviral activity of ACA in cell cultures warrants further evaluation in other virus disease models (Fig. 3). Type I interferon receptor–deficient A129 mice were infected with ZIKV-PR (a strain of the ZIKA virus originally isolated from a traveler to Puerto Rico) and treated with either ACA (1 mg/kg) or DMSO by subcutaneous administration. Mice receiving one dose of ACA therapy showed a remarkably better survival rate (100% versus 0%) and mean body weight (Fig. 3, A and B). Moreover, ZIKV titer was undetectable in the brains of ACA-treated group, whereas

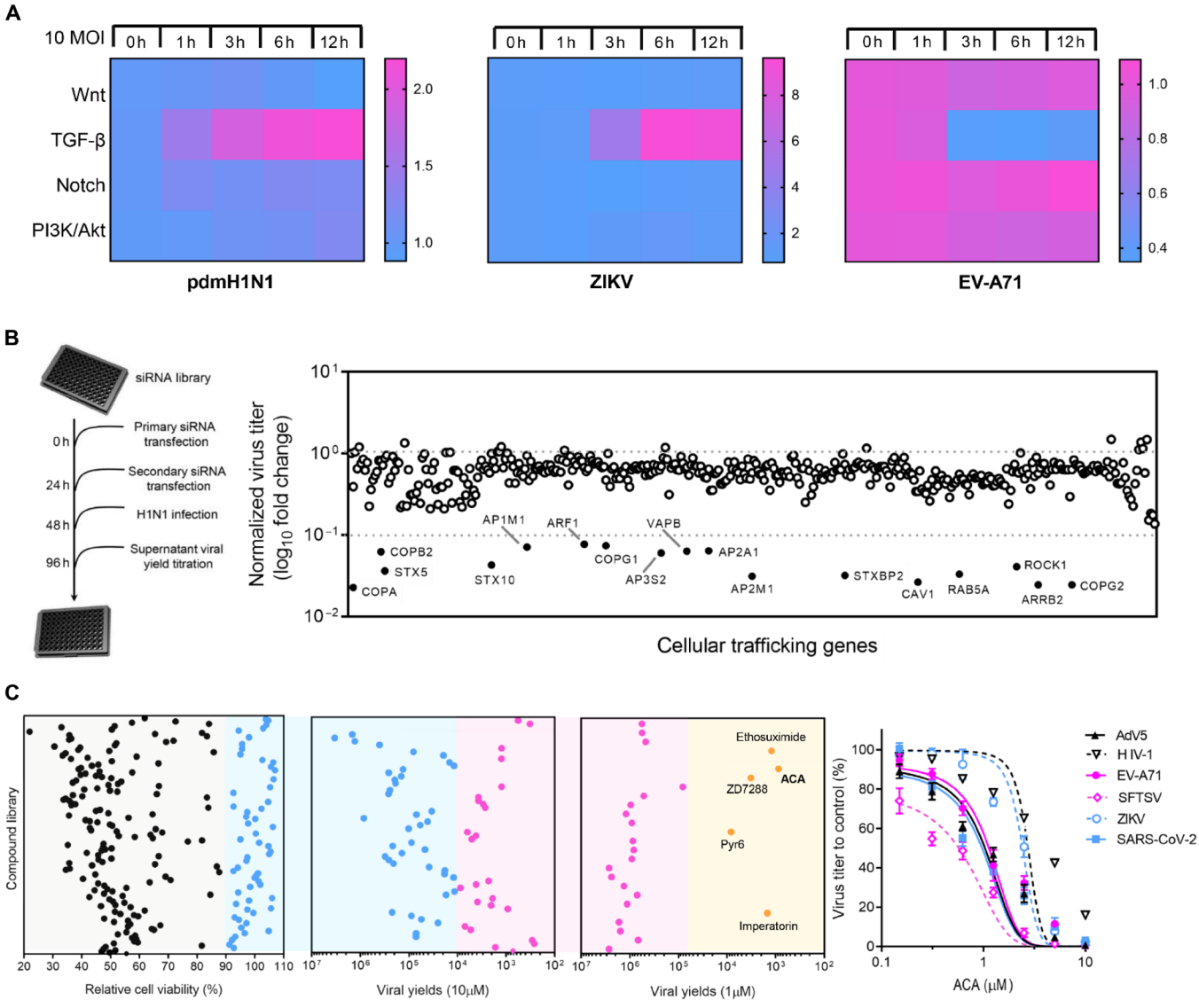

Fig. 1. Intracellular trafficking pathways are vulnerable and druggable for antiviral intervention. (**A**) Time-course responses of cell fate determination pathways upon infection of different viruses. Luciferase reporter gene assays reflecting the activity of Wnt, TGF-β, Notch, and PI3K/Akt signaling were performed on the pdmH1N1-infected HBTEC, ZIKV-infected human fibroblasts, and EV-A71–infected human neural progenitor cells, respectively. The results are shown as a heatmap. (**B**) RNA interference (RNAi) screening identified genes essential for pdmH1N1 virus replication. Left: Experimental workflow that was performed in human lung epithelial A549 cells with 0.1 MOI virus infection. Right: Among 142 membrane and cellular trafficking genes, individually knockdown of 17 genes (black dots) can suppress virus replication for >1-log magnitude when comparing with the scramble–small interfering RNA (siRNA) control. (**C**) Small-molecule compound library screening identified ACA as a broad-spectrum antiviral in vitro. A membrane transporter/cellular trafficking library was primarily screened in pdmH1N1-infected Madin-Darby canine kidney (MDCK) cells (0.01 MOI and 48 hpi) through cell protection assays (box 1, blue dots indicated >90% cell viability), followed by secondary screening using viral load reduction assays (box 2, magenta dots indicated >3 logs of viral load reduction applying 10 μM drug concentration) and tertiary screening (box 3, yellow dots indicated >2 logs of viral load reduction using 1 μM drug concentration). ACA was prioritized due to its broad-spectrum antiviral efficacy. Shown in the last panel are the antiviral effects against six different viruses as indicated. Shown are the plaque-forming unit (PFU) or 50% tissue culture infectious dose ($TCID_{50}$) or OD_{450} (optical density at 450 nm) value of indicated concentrations relative to controls in the absence of compound (%).

that of DMSO group was generally 4 logs higher (Fig. 3C). Less histopathologic changes of meningoencephalitis and ZIKV-NS1 antigen expression were observed (Fig. 3D). Furthermore, intranasal ACA (0.2 mg/kg, i.n.) provided good protection against lethal challenge with 500 PFU of MERS-CoV in human dipeptidyl peptidase 4 (hDPP4)–transgenic mice, whereas all DMSO-treated mice died on or before day 8 after challenge (100% versus 0%; Fig. 3E). Body weight loss in the DMSO-treated mice began since 5 dpi, while that of the ACA-treated group continued to increase (Fig. 3F). About 2 logs lower lung tissue virus titer was detected in the ACA group (Fig. 3G). Inflammatory infiltration and MERS-CoV-NP antigen expression in the lung tissues were substantially reduced after ACA treatment (Fig. 3H). Thus, ACA also exhibited broad-spectrum antiviral efficacy in vivo.

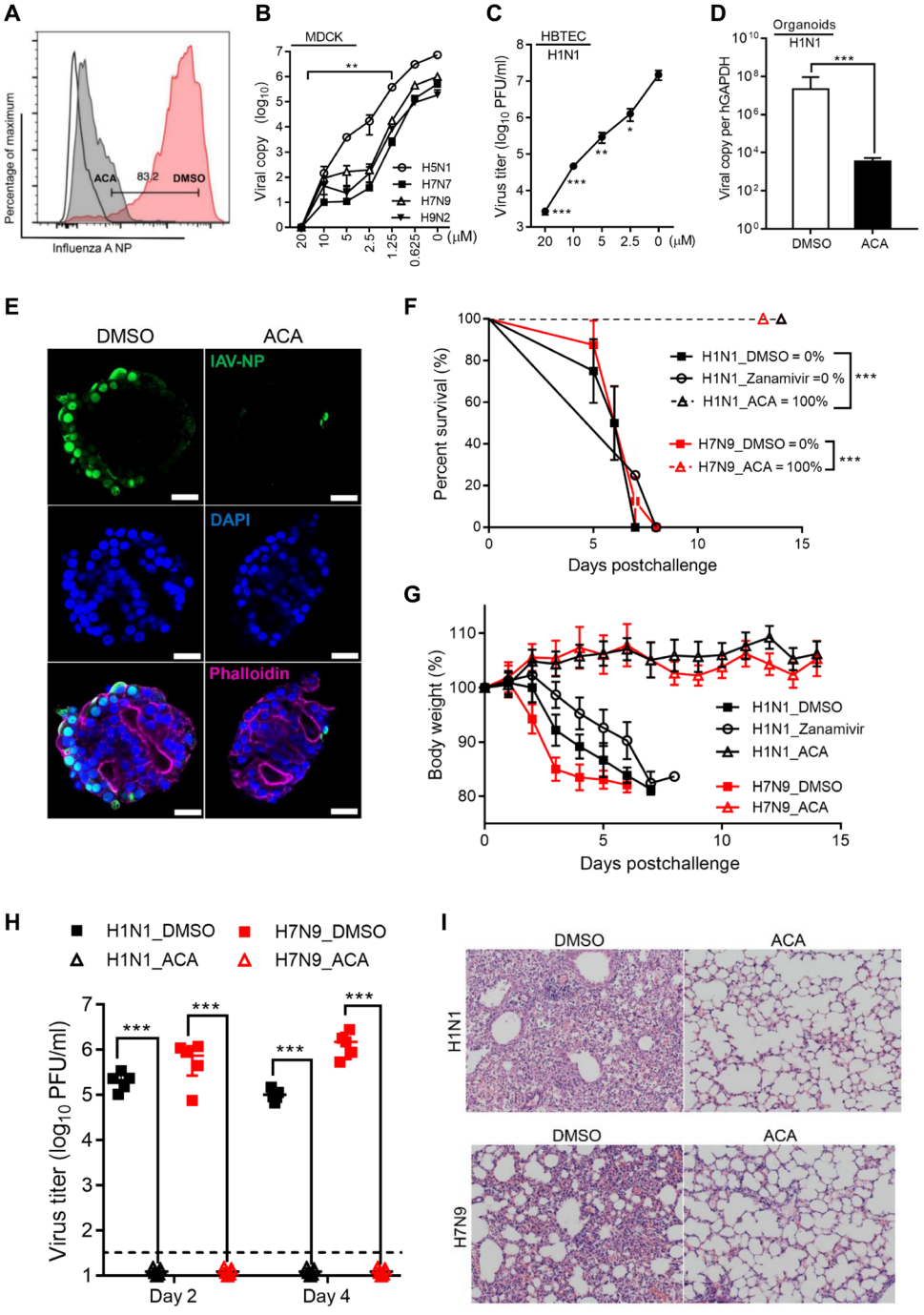

Fig. 2. Anti–influenza activity of ACA in vitro and in vivo. (**A**) ACA reduced influenza A NP–positive MDCK cells as quantitated by flow cytometry. (**B**) ACA exhibited cross-subtype anti–influenza activity including influenza A H5N1, H7N7, H7N9, and H9N2 viruses. $^{**}P < 0.01$ by one-way analysis of variance (ANOVA). (**C**) ACA suppressed pdmH1N1 replication in HBTECs (0.01 MOI). One-way ANOVA was used for comparison with the dimethyl sulfoxide (DMSO)–treated group (0 μM). $^{*}P < 0.05$. (**D**) ACA (10 μM) showed anti–influenza activity in differentiated human AOs. Shown is the intracellular viral gene copies normalized by glyceraldehyde-3-phosphate dehydrogenase (GAPDH). $^{***}P < 0.001$ by Student's *t* test. (**E**) Representative 2D images of human AOs, after immunofluorescence staining for viral NP (green), 4′,6-diamidino-2-phenylindole (DAPI) (blue, for nucleus), and Phalloidin (magenta, for cellular membrane), were examined with confocal microscopy. Scale bars, 20 μm. (**F** to **I**) ACA provided full protection against lethal challenge with influenza A H1N1 (black lines) or H7N9 (red lines) viruses. The mice were treated with intranasal ACA (open triangles), zanamivir (open circle), or 0.5% DMSO (closed squares) for one dose starting 1 hour after challenge. (F) Survival and clinical disease were monitored for 14 days or until death. $^{***}P < 0.001$ by log-rank (Mantel-Cox) tests. (G) Daily body weights of surviving mice. (H) Lung tissues ($n = 5$ per group) were collected for detection of viral titers using plaque assay at 2 and 4 dpi, respectively. A value of 10 to 15 PFU/ml was assigned for any titer below the detection limit (the dotted line). (I) Representative histological sections of lung tissues (4 dpi) from the indicated groups with hematoxylin and eosin (H&E) staining. Greater alveolar damage and interstitial inflammatory infiltration were present in the DMSO group. Magnification: ×200.

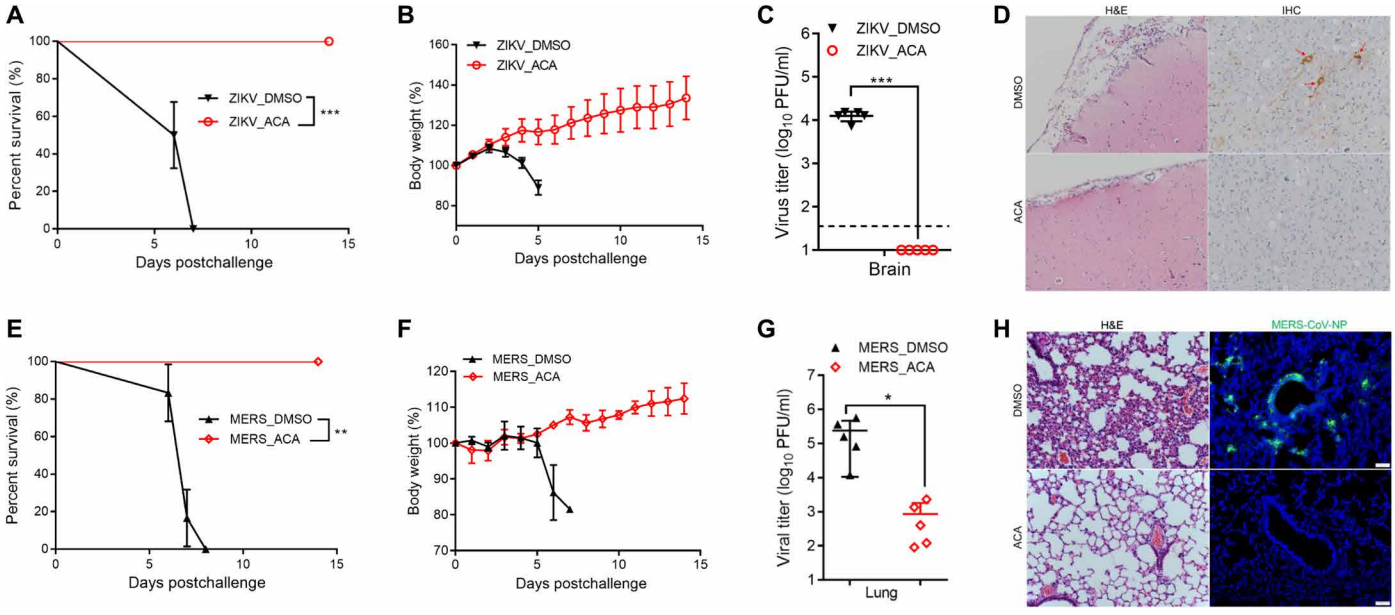

Fig. 3. ACA shows broad-spectrum antiviral activity in vivo. (**A** to **D**) ACA conferred protection against lethal challenge of ZIKV. Four- to 6-week-old A129 mice were inoculated subcutaneously with 1×10^6 PFU of ZIKV-PR under anesthesia. Each mouse received one dose of subcutaneously administered ACA (1 mg/kg) or 0.5% DMSO in PBS at 1 hpi. The mice were monitored daily for (A) survival rate and (B) body weight change. (C) Five mice in each group were euthanized at 6 dpi, and brain tissues were harvested for vial titer determination by plaque assay. The dotted line indicates the lower detection limit of plaque assay (***$P < 0.001$; for the purpose of statistical analysis and clarity, a value of 10 to 15 PFU/ml was assigned for any titer below the detection limit). (D) Histopathologic and immunohistochemistry (IHC) analyses of the brain samples at 6 dpi indicated less severe meningitis (by H&E, ×200) and less virus infected cells as indicated by ZIKV NS1 antigen staining (red arrows, by IHC, ×200 magnification) after ACA treatment. (**E** to **H**) ACA protected human dipeptidyl peptidase 4 (hDPP4) transgenic mice from MERS-CoV infection. The hDPP4 mice were intranasally inoculated with 500 PFU of MERS-CoV and intranasally treated by ACA or 0.5% DMSO for one dose starting 1 hpi. Shown are (E) survival rate, (F) mean body weight, (G) lung viral titer at 2 dpi ($n = 5$ per group), and (H) representative lung tissues stained by H&E and anti–MERS-CoV-NP immunofluorescence. The staining suggested less inflammatory cell filtration (by H&E, ×200 magnification) and less virus infected cell antigens (by immunofluorescence (IF) staining, green fluorescence) as detected in ACA-treated mouse lungs. Results are presented as mean values ± SD. Differences in survival rates were compared using log-rank (Mantel-Cox) tests and viral titer by Student's *t* test. ***$P < 0.001$, **$P < 0.01$, *$P < 0.05$.

ACA targets host AP2M1 protein

ACA is known as a phospholipase A2 (PLA2) inhibitor and transient receptor potential (TRP) channel blocker (*15*), but such mechanisms for suppressing viral replication were excluded (fig. S3). To explore its actual mechanism of antiviral action, we performed time-of-addition assays to investigate how ACA interferes with different phases of the viral replication cycle. ACA did not inactivate virus particles nor affect virus attachment to host cell surface (fig. S4). To dissect the postvirus attachment steps, we quantified three types of influenza virus RNA [vRNA, complementary RNA (cRNA), and mRNA] at different time points after virus internalization. Distinct dynamics of vRNA, cRNA, and mRNA synthesis were observed in the control groups, while all viral RNA types in ACA groups remained at the baseline level within 0 to 5 hpi of ACA addition (Fig. 4A). The result suggested that ACA functions within 1.5 hours after internalization before cRNA synthesis and therefore may inhibit virus endocytosis and nuclear import or blocking viral ribonucleoprotein (vRNPs) activity directly. Because LysoTracker red assay indicated that the acidification of endosomal compartments was not affected, the uncoating of vRNA for release into cytoplasm upon virus fusion was unlikely to be blocked by ACA (fig. S3C). Hence, we directly tracked the location of the vRNA within the incoming vRNPs (Fig. 4B). At indicated time points, cells were processed and stained for the negative-stranded NP vRNA of PR8 using a specific RNA probe set (red). In the DMSO-treated cells, the dominant nuclear import of vRNA was detected by 1 hpi, followed by predominant cytosol location between 1.5 and 2 hpi. By comparison, the nuclear vRNA signal was rarely observed after ACA addition throughout the time course. Therefore, ACA may inhibit IAV replication by blocking vRNA nuclear import.

To ascertain the target of ACA, we developed an unbiased drug target–elucidating platform that integrates Click-chemistry, WaterLOGSY, and protein ID techniques using liquid chromatography–tandem mass spectrometry (LC-MS/MS), namely, CWID (Fig. 4, C and D). First, click-chemistry was applied to introduce an azido group to ACA (azido-ACA), without compromising its antiviral efficacy (Fig. 4C, middle). With an azido-reactive fluorescent dye (DyLight 488), azido-ACA but not ACA was visualized in both the cytosol and nucleus (Fig. 4C, right). Next, WaterLOGSY, a ligand-binding determination method through observing the nuclear overhauser effect, was applied for primary nuclear magnetic resonance (NMR) screening of cellular fragments that exhibited high binding affinity to ACA. Virus-infected MDCK cells were fractionated by gel filtration chromatography, followed by WaterLOGSY to capture the ACA-interacting signals, individually (Fig. 4D, middle). Iterative rounds of subfractionation and WaterLOGSY were performed to obtain the maximally separated fraction with detectable ACA signals. Subsequently, the bound form of fraction-azido-ACA mixture was stained by DyLight 488 and subject to electrophoresis in a native polyacrylamide gel electrophoresis. A specific band indicating the

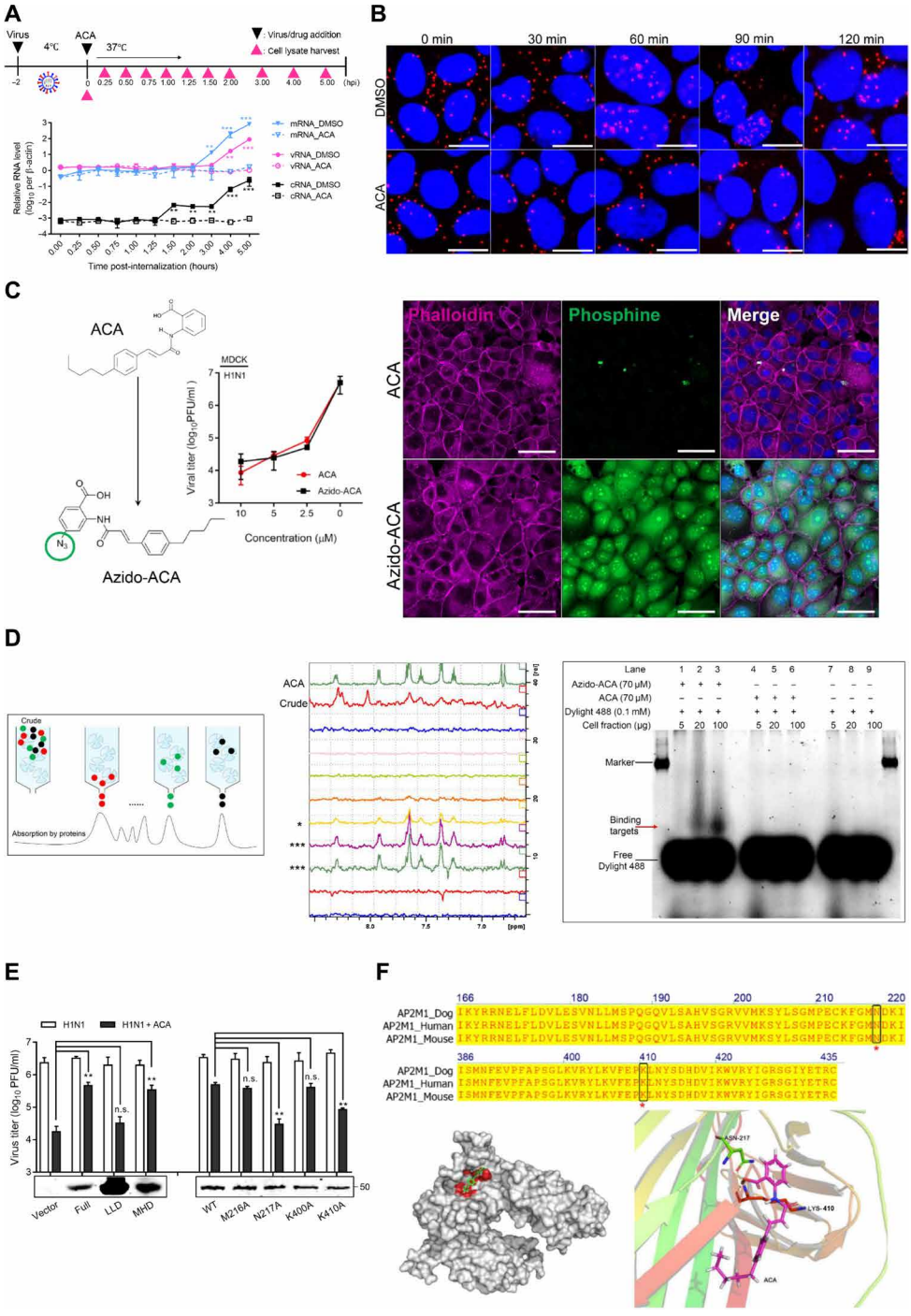

Fig. 4. ACA targets host AP2M1 protein. (**A**) ACA blocked the initiation of pdmH1N1 virus replication cycle. Cell lysate were collected for virus mRNA (blue lines), vRNA (magenta lines), and cRNA (black lines) quantification as indicated. Student's *t* test for each RNA type and corresponding time point. (**B**) ACA inhibited nuclear import of the IAV vRNA. Synchronized H1N1 infection were performed on MDCK cells (50 MOI). Cells were fixed at the indicated time points and hybridized with RNA probes against the IAV negative-stranded NP vRNA (red) and stained for DNA (blue), examined by confocal microscopy. Images are representative of three independent experiments. Scale bars, 10 μm. (**C** and **D**) Click chemistry/WaterLOGSY/protein ID (CWID) platform for identification of drug-binding targets. (C) Click-chemistry: chemical structure of azido-ACA showing the location of azido group (green circle) on ACA. Cellular distribution of azido-ACA is shown (green), whereas ACA was used as a negative control due to the lack of phosphine-reactive azido group. Scale bars, 50 μm. (D) WaterLOGSY-guided cellular fractionation was subjected to analysis for ACA-featured NMR spectra. "*" and "***" indicate mild and strong binding signals, respectively. The native polyacrylamide gel electrophoresis gel photo shows the selected cell fraction as detected by a fluorescent image analyzer. Red arrow indicates the specific azido-ACA–binding fragment. (**E**) Mutagenesis analysis of AP2M1 to rescue pdmH1N1 virus replication against ACA. Full-length AP2M1 (full), longin-like domain (LLD), MHD, and mutant AP2M1 were transfected to MDCK cells before virus infection and ACA treatment. One-way ANOVA. $^{**}P < 0.01$; n.s, not significant. (**F**) Partial sequence alignment of human, mouse, and dog AP2M1 is shown. N217 and K410, the key residues for ACA binding, are highlighted with a box. The predicted interaction surfaces on AP2M1 (red) are shown, while ACA (green) is displayed in stick and mesh representation.

protein-compound complex was visualized in the azido-ACA group, while it was absent in the ACA or cell lysate–only group (Fig. 4D, right). Gel plug of the target band was collected for LC-MS/MS, which identified eight candidate proteins that were physically associated with azido-ACA. To validate their biological function besides binding, individual open reading frame (ORF) clone was overexpressed to overcome the inhibition of virus replication by ACA. Apparently, only ectopic expression of AP2M1 notably rescued pdmH1N1 growth despite the presence of ACA, indicating AP2M1 being one of the most likely targets that accounts for ACA's mode of action (fig. S5).

AP2M1 consists of an N-terminal (~150 amino acids) longin-like domain (LLD) and a C-terminal (170 to 434 amino acids) mu homology domain (MHD). Functionally, we demonstrated that overexpression of either full-length AP2M1 or MHD enhanced pdmH1N1 replication for about 1.5 logs despite adding ACA, whereas overexpressed LLD did not antagonize ACA's antiviral activity (Fig. 4E, left bar charts). Thus, MHD harbors sites of ACA interaction. Amino acid residues of MHD are conserved across the human, dog, and mouse AP2M1, which is in line with the broad-spectrum antiviral coverage of ACA in different species of cells and mouse models. Molecular docking predicts that ACA interacts mainly with AP2M1 through four amino acids, M216, N217, K400, and K410 (Fig. 4F). Our mutational experiment showed that substitution in N217A or K410A failed to antagonize the ACA's antiviral activity when compared with that of the M216A, K400A, or wild-type (WT) AP2M1 (Fig. 4E, right bar charts). Collectively, ACA targets host AP2M1 by interacting with its N217 and K410 residues.

Host AP2M1 is exploited by multiple families of virus via their proteins harboring YxxØ binding motif

The antiviral spectrum of ACA spans across enveloped (ZIKV) and nonenveloped (EV-A71), retro (HIV-1), and nonretro (IAV), as well as DNA (AdV-5) and RNA (MERS-CoV) viruses (fig. S2A). Thus, AP2M1 must be broadly exploited during life cycles of many viruses. First, we excluded the possibility that ACA affected phosphorylation of AP2M1 (fig. S6), which has been approved to be antiviral effective by Bekerman *et al.* (*16*). Subsequently, to find the specific virus protein interacting with host AP2M1, we performed an immunoprecipitation (IP) screening of viral ORF clones. Previous host-IAV interactome suggested M1, hemagglutinin (HA), PB2, and NP as the potential AP2M1-binding proteins without individual validation (*17*). After coexpression of each viral gene and HA-tagged AP2M1 in human embryonic kidney (HEK) 293T cells, only NP could be detected in the IP complex, but adding ACA markedly diminished the target NP band (fig. S7A). Using the same approach, we identified the ZIKV-NS3, MERS-CoV-NP, and EV-A71-2C as the interacting partners of AP2M1 (fig. S7, B to D).

AP2M1 is known to mediate sorting of cargo proteins harboring YxxØ or dileucine motifs (*18*). Using bioinformatic methods, we found that YxxØ but not dileucine motif was consistently present in the implicated AP2M1-binding viral proteins. The YxxØ motifs are highly conserved in specific proteins across many virus families including the NP of *Orthomyxoviridae*, Gag of *Retroviridae*, NP of *Bunyaviridae*, NS3 of *Flaviviridae*, NP of *Coronaviridae*, 2C of *Picornaviridae*, and Core Protein V of *Adenoviridae* by bioinformatics (Fig. 5A). To determine whether ACA blocked the AP2M1 YxxØ-binding site, we developed a competitive enzyme-linked immunosorbent assay (ELISA). As positive controls, addition of either nonlabeled YxxØ motif peptide DYQRLN or the low-affinity mutant D176A AP2M1 (*19*) resulted in diminished binding signal during binding of biotin-YxxØ substrate to the immobilized His-AP2M1. ACA pretreatment notably reduced AP2M1/biotin-YxxØ interaction (Fig. 5B). To explore whether the YxxØ-binding pocket is a druggable target for antiviral therapy, we also tested tyrphostin A23, which blocks the tyrosine-binding pocket of AP2M1 (*20*). At nontoxic concentrations, Tyrphostin A23 suppressed a panel of viruses including pdmH1N1, MERS-CoV, EV-A71, and ZIKV (Fig. 5C). Last, the effect of AP2M1 gene depletion on viral replication was investigated. AP2M1 knockout led to dramatic viral load reduction in pdmH1N1-infected 293T cells, EV-A71–infected rhabdomyosarcoma (RD) cells, ZIKV-infected Huh7 cells, and MERS-CoV–infected Huh7 cells (Fig. 5D). Together, AP2M1/YxxØ interaction is a critical step in the viral replication cycle and druggable for antiviral intervention.

AP2M1/YxxØ interaction facilitates virus trafficking beyond endocytosis to promote viral replication

Next, we asked the functional roles of AP2M1/YxxØ interaction during viral replication cycles using IAV, EV-A71, and ZIKV-NS3 as three representative viruses. Nuclear import of IAV NP through the nuclear pore complex is a prerequisite for efficient vRNP translocation and subsequent genome replication, while our data clearly showed that ACA impaired vRNA nuclear import and AP2M1/NP binding (Fig. 4B and fig. S7A). Thus, we postulated that AP2M1 facilitated NP import from cytoplasm to the nucleus via recruiting the NP-YxxØ motif. To quantify the retardation of NP import in AP2M1$^{-/-}$ 293T cells, cells were infected with 10 MOI IAV, and cycloheximide (CHX) was added to inhibit protein synthesis. Crude cell lysate was separated into nuclear (Nuc) and cytoplasmic (Cyto) fractions at 2 hpi (Fig. 5E). In WT cells, AP2M1 protein was mainly detected in cytoplasm, whereas considerably more viral NPs were found in nucleus. However, in AP2M1$^{-/-}$ cells, viral NP was predominantly found in the cytoplasmic fraction instead. Since the only source of NP protein was from the incoming vRNPs after CHX treatment, the finding suggested that AP2M1 facilitates the nuclear import of incoming vRNPs. To provide direct evidence for a role of AP2M1 in mediating intracellular NP trafficking that beyond endocytosis, we monitored the cotrafficking of NP–green fluorescent protein (GFP) with AP2M1-mCherry using live cell imaging. GFP/mCherry signal was found largely in the host nucleus (movie S1). Upon ACA treatment, NP resides predominantly in the cytosol, and the mobility of the AP2M1-associated NP puncta (yellow) was reduced remarkably, which suggested diminished NP trafficking via AP2M1 (Fig. 5F and movie S2). Nevertheless, most positive-stranded RNA viruses replicate their genomes on the cytoplasmic endoplasmic reticulum (ER) membrane without entering the nucleus. For example, EV-A71-2C and ZIKV-NS3 proteins induce the formation of viral RNA replication complex by trafficking predominantly to the ER membrane (*21*). In the context of synchronized viral infection, we demonstrated by confocal imaging the extensive localization of IAV-NP and nucleus, so were the EV-A71-2C and ZIKV-NS3 in ER, respectively. After ACA treatment, however, reduced rates of colocalization were revealed in all three representative viruses (89% versus 12% for IAV-NP/nucleus; 63% versus 21% for EV-A71-2C/ER; 95% versus 56% for ZIKV-NS3/ER; Fig. 5G). In summary, these results confirmed an important role of AP2M1 in trafficking viral proteins beyond endocytosis.

To bridge the AP2M1-mediated trafficking and virus replication, we rescued the recombinant IAV with a series of point mutations on two NP-YxxØ locations, i.e., Y296-V299 (YSLV) and Y385-I388

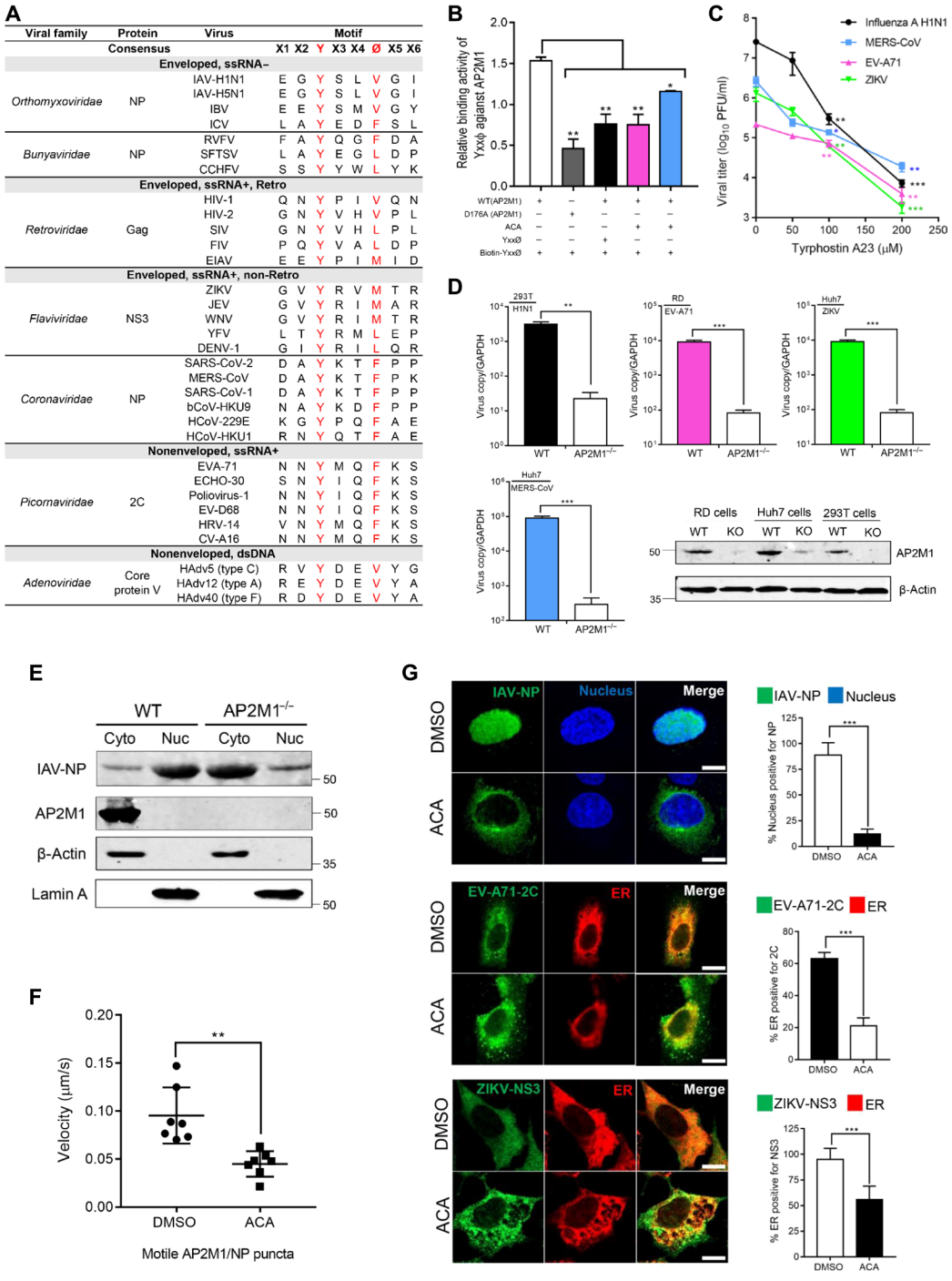

Viral family	Protein	Virus	Motif							
	Consensus		X1	X2	Y	X3	X4	Ø	X5	X6
Enveloped, ssRNA−										
Orthomyxoviridae	NP	IAV-H1N1	E	G	Y	S	L	V	G	I
		IAV-H5N1	E	G	Y	S	L	V	G	I
		IBV	E	E	Y	S	M	V	G	Y
		ICV	L	A	Y	E	D	F	S	L
Bunyaviridae	NP	RVFV	F	A	Y	Q	G	F	D	A
		SFTSV	L	A	Y	E	G	L	D	P
		CCHFV	S	S	Y	Y	W	L	Y	K
Enveloped, ssRNA+, Retro										
Retroviridae	Gag	HIV-1	Q	N	Y	P	I	V	Q	N
		HIV-2	G	N	Y	V	H	V	P	L
		SIV	G	N	Y	V	H	L	P	L
		FIV	P	Q	Y	V	A	L	D	P
		EIAV	E	E	Y	P	I	M	I	D
Enveloped, ssRNA+, non-Retro										
Flaviviridae	NS3	ZIKV	G	V	Y	R	V	M	T	R
		JEV	G	V	Y	R	I	M	A	R
		WNV	G	V	Y	R	I	M	T	R
		YFV	L	T	Y	R	M	L	E	P
		DENV-1	G	I	Y	R	I	L	Q	R
Coronaviridae	NP	SARS-CoV-2	D	A	Y	K	T	F	P	P
		MERS-CoV	D	A	Y	K	T	F	P	K
		SARS-CoV-1	D	A	Y	K	T	F	P	P
		bCoV-HKU9	N	A	Y	K	D	F	P	P
		HCoV-229E	K	G	Y	P	Q	F	A	E
		HCoV-HKU1	R	N	Y	Q	T	F	A	E
Nonenveloped, ssRNA+										
Picornaviridae	2C	EVA-71	N	N	Y	M	Q	F	K	S
		ECHO-30	S	N	Y	I	Q	F	K	S
		Poliovirus-1	N	N	Y	I	Q	F	K	S
		EV-D68	N	N	Y	I	Q	F	K	S
		HRV-14	V	N	Y	M	Q	F	K	S
		CV-A16	N	N	Y	M	Q	F	K	S
Nonenveloped, dsDNA										
Adenoviridae	Core protein V	HAdv5 (type C)	R	V	Y	D	E	V	Y	G
		HAdv12 (type A)	R	E	Y	D	E	V	Y	A
		HAdv40 (type F)	R	D	Y	D	E	V	Y	A

Fig. 5. Host AP2M1 is exploited by multiple viruses via the viral protein YxxØ motif. (**A**) A summary of virus protein YxxØ motif interacting with host AP2M1 proteins. (**B**) Competitive ELISA showing the blockade of AP2M1 and biotin-YxxØ peptide after ACA addition. The low binding affinity mutant D176A was taken as a control. One-way ANOVA. $*P < 0.05$ and $**P < 0.01$. (**C**) A known AP2M1-YxxØ blocker Tyrphostin A23 exhibited broad-spectrum antiviral activity. Shown are the antiviral effects against four different viruses as indicated. One-way ANOVA when compared with the 0 μM group (0.1% DMSO). (**D**) CRISPR knockout of AP2M1 reduced pdmH1N1, EV-A71, ZIKV, and MERS-CoV replication. Viral load in the cell lysate ($n = 3$) was evaluated by quantitative reverse transcription polymerase chain reaction (RT-qPCR). Student's *t* test. (**E**) AP2M1$^{-/-}$ and WT 293T cells were treated with CHX before virus infection (10 MOI). Nuclear (Nuc) and cytoplasmic (Cyto) fractions were separated and detected at 2 hpi by Western blotting. (**F**) A549 cells transfected with GFP influenza–NP and mCherry-AP2M1 were incubated with DMSO or ACA for 24 hours. Live cell imaging was performed, and motile AP2M1/NP puncta were tracked (movies S1 and S2). Shown is the average velocity of trackable puncta within the overall distance traveled. Student's *t* test. (**G**) AP2M1 facilitates the viral protein localization. Synchronized infections were used throughout the experiments. Colocalization was quantified using ImageJ (JACoP) colocalization software and Manders' colocalization coefficients (MCCs). Bar charts indicate mean MCC values represented as percent colocalization (the fraction of green intensity that coincides with blue intensity in the case of IAV-NP/nucleus and the fraction of green intensity that coincides with red intensity in the case of EV-A71-2C/ER and ZIKV-NS3/ER) ± SD (error bars, $n = 10$ to 15). Scale bars, 10 μm. $***P < 0.001$ by Student's *t* test.

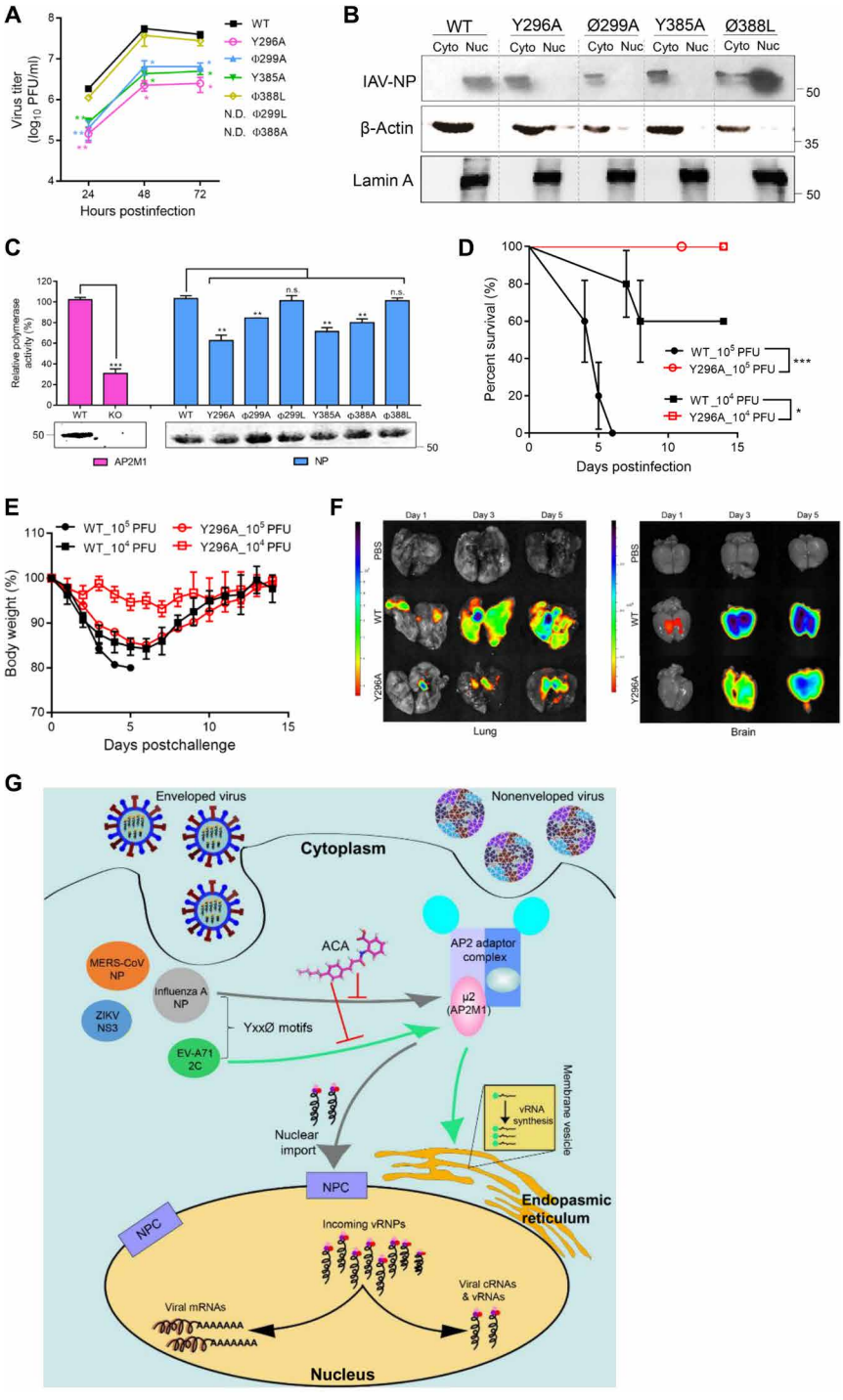

Fig. 6. Host AP2M1-mediated virus trafficking is essential to initiate their replication cycles. (**A**) Effects of virus NP-YxxØ substitutions on virus growth and replication. Recombinant viruses were subject to multiple-cycle replication assays in A549 cells . N.D indicates failed rescue in three independent experiments. (**B**) Effects of virus NP-YxxØ substitutions on IAV NP nucleus import. A549 cells were treated with CHX before infection with WT and mutant viruses (10 MOI). Nuclear (Nuc) and cytoplasmic (Cyto) fractions were separated at 2 hpi for Western blotting to quantify the NP amount. Human β-actin and Lamin A were used for normalization of Cyto and Nuc, respectively. (**C**) Disruption of host AP2M1/ virus NP binding abolished the replication and transcriptional activity of influenza A polymerase. Shown are the relative polymerase activities with AP2M1 knockout (magenta bars) or NP mutants on YxxØ sites (blue bars). AP2M1 KD efficiency and NP overexpression were detected by Western blotting. Student's *t* test . (**D** to **F**) Growth of WT and mutant (Y296A) GFP virus in a mouse model. BALB/c mice were intranasally infected with 10^5 or 10^4 PFU of the indicated viruses. Shown are the (D) survival rate and (E) body weight change. (F) Three mice from each 10^5 PFU-infected group were euthanized on 1, 3, and 5 dpi for analysis of in vivo dynamics after GFP virus infection. (**G**) Proposed model for host AP2M1-mediated intracellular trafficking of different viruses. Various viral proteins as indicated are commonly recruited by the mu subunit of host membrane trafficking AP2 adaptor complex (i.e., AP2M1 or μ2) through recognizing the viral YxxØ motif, while ACA disrupts these distinct steps of the viral life cycle.

(YWAI) (fig. S8). Mutagenesis includes two Y/A substitutions (Y296A and Y385A), two Ø/A substitutions (V299A and I388A), and two Ø/L substitutions (V299L and I388L). The growth rates of the Y296A, Y385A, and Ø299A mutant viruses were attenuated for >1-log in each time point, while Ø388L mutant virus exhibited similar replication kinetics as that of the WT (Fig. 6A). The results not only indicated the critical role of NP-YxxØ in determining the virus fitness but also that YxxØ is functionally interchangeable within homologous Ø signals (i.e., I388L substitution). However, we were unable to rescue the recombinant viruses containing Ø299L or Ø388A mutation for three independent experiments. To validate whether the reduction of IAV replication was due to the decreased NP nucleus entry, a step which is beyond AP2M1-mediated endocytosis, the successfully rescued WT and mutant IAV were used to infect A549 cells, followed by measuring NP in both the cytosol and nucleus at 2 hpi. Apparently, NP was not detectable in the host nucleus after infection of IAVs carrying Y296A, Y385A, and Ø299A NP substitutions, while Ø388L mutant virus exhibited similar amount of NP as that of the WT (Fig. 6B). As expected, influenza polymerase luciferase reporter activity from both Ø/L mutants (Ø299L and Ø388L) was similar to that of WT, whereas all Y/A (Y296A and Y385A) and Ø/A (Ø299A and Ø388A) mutants displayed reduced polymerase activity. Moreover, AP2M1 gene depletion reduced the polymerase activity by >75% (Fig. 6C). The results suggested that amino acid residues of NP-YxxØ motif determined the IAV polymerase activity via modulating the NP nuclear import.

Furthermore, we extended the analysis in vivo and selected the most attenuated Y296A substitution for a full comparison with the WT. BALB/c mice were challenged with two doses of WT-H5N6-GFP (WT) and Y296A-H5N6-GFP (Y296A) viruses, respectively. Survival of Y296A-challenged (10^5 PFU) group (100% versus 0% versus 60%) was obviously better than those of WT-challenged (10^5 PFU) group and WT-infected (10^4 PFU) group (Fig. 6D). Mice in the 10^5 PFU Y296A group displayed similar weight loss to those of the 10^4 PFU WT-infected group but rebounded after 7 dpi, whereas the 10^4 PFU Y296A group displayed mild body weight loss (<5%) throughout the infection (Fig. 6E). Taking advantage of the GFP reporter feature of the recombinant IAV for in vivo dynamic analysis, we examined lung and brain samples from infected mice at different dpi. Apparently, spreading of WT virus deeper into the bronchioles and possibly alveoli were detected since 3 dpi, while GFP signal from Y296A mutant virus was confined to regions around the initial sites of infection around the trachea and bronchi, indicating limited virus spread (Fig. 6F, left). In line with the reported occurrence of neurological symptoms in highly pathogenic H5-infected animals, extensive GFP signals could be visualized in WT virus–infected mouse brain as early as 3 dpi. In contrast, the Y296A group illustrated reduced GFP intensity throughout the time points (Fig. 6F, right). These data provided evidence that a single Y296A substitution in NP-YxxØ motif notably restricted IAV replication in vivo. Together, host AP2M1/virus YxxØ interaction is critical for intracellular virus trafficking to the sites of replication/transcription beyond the step of endocytosis, thereby facilitating viral replication (Fig. 6G).

DISCUSSION

Viruses exploit distinct receptors to facilitate cell entry and to evade a hostile extracellular environment that would otherwise abrogate infection. Within the intracellular settings, we demonstrated a conserved host AP2M1/virus YxxØ interaction that is commonly harnessed by different viruses during intracellular trafficking but beyond the well-defined CME process (Fig. 6G). Using ACA as a tool compound, we developed the CWID platform and identified the YxxØ-binding pocket of the host AP2M1 as a previously unidentified target for broad-spectrum antiviral development, which is different from the previous antiviral strategy to block AP2M1 phosphorylation (fig. S6). Although the AP2M1$^{-/-}$ mice is lethal (*22*), the AP2M1$^{-/-}$ cell line is not susceptible to the infections of IAV, EV-A71, MERS-CoV, and ZIKV (Fig. 5D). On the virus side, YxxØ motif determines the capacity of NP nuclear translocation and therefore affects IAV fitness (Fig. 6, A to F).

The outcome of a viral infection with respect to cellular fate is a fundamental aspect of viral biology. We find that TGF-β signaling is a cell fate determinant pathway with broad relevance of multiple viruses, and these viruses use AP2M1 as a common intermediate for intracellular trafficking but beyond endocytosis: First, by using live IAV infection, vRNA was visualized in the perinuclear region but within the cytosol, indicating that the IAV entry process has not been affected by ACA (Fig. 4B); after endocytosis, however, NP were predominantly excluded from the nucleus of AP2M1$^{-/-}$ cells, suggesting that AP2M1 was indispensable for IAV-NP nuclear localization (Fig. 5E). The role of AP2M1 associated with hepatitis C virus (HCV) entry and assembly has been defined (*23*, *24*). Our study further demonstrated the versatility and broadness of AP2M1 to cotraffic with several other internal viral proteins for the completion of their replication cycles. Represented by IAV (enveloped and negative-stranded), EV-A71 (nonenveloped), and ZIKV (enveloped and positive-stranded), we demonstrated that recruitment of YxxØ-harboring IAV-NP, EV-A71-2C, and ZIKV-NS3 proteins by AP2M1 was functionally related in their correct localization as to facilitate viral genome replication. Strategically, AP2M1 was harnessed by viral NP for efficient nuclear entry, thereby promoting polymerase activity. Substitutions introduced in the viral YxxØ motif as Y to A or Ø to A greatly diminished virus growth in vitro and in vivo. Since the virulence of NP Y296A mutant virus was attenuated, strategic usage of IAV strains containing this or other mutants as vaccines might be evaluated in the future. In the case of EV-A71 and ZIKV, AP2M1 was required for efficient transportation of 2C and NS3 proteins to the ER membrane so that their genome replication can occur. Furthermore, the essentiality of AP2M1 during virus replication was validated in the context of multiple viruses including pdmH1N1, EV-A71, ZIKV, and MERS-CoV infections (Fig. 5D). Together, AP2M1 might be universally exploited by different viruses to complete their replication cycle after cell entry.

The architecture of AP2 has to undergo a large conformational change from a "closed," cargo-inaccessible state to an "open" structure so as to expose the YxxØ binding site, which is regulated by AP2-associated protein kinase 1 and cyclin G–associated kinase (*7*). Although it has been reported that inhibitors of this kinase (e.g., sunitinib and erlotinib) can inhibit RNA viruses including dengue, Ebola, and HCV, the in vivo antiviral potency of ACA (100% survival in IAV, ZIKV, and MERS-CoV mouse models) is much better than that of sunitinib [37% protection in dengue virus (DENV) and 30% in ebola virus (EBOV) mouse models] or erlotinib (conferring no protection in either the DENV or EBOV mouse model) (*16*). Targeting directly the YxxØ-binding pocket instead of the T156 AP2M1 phosphorylation site, our study not only extends the therapeutic window beyond the conformational change of AP2M1, which is transient and mediated by kinase activity, but also opens up another

synergistic antiviral approach by combining ACA with other inhibitors including sunitinib or erlotinib. A major roadblock to translating protein kinase inhibitors into clinical development is the doubt about their poor selectivity, which is largely a consequence of the highly conserved ATP-binding site shared by all protein kinases (*25*). Disruption of PPIs, as exemplified in our study, however, is usually highly specific against the binding interface, which has less concern about cytotoxicity. Occupation of AP2M1 YxxØ-binding pocket by using Tyrphostin A23 blocked the replication of multiple viruses (Fig. 5C). Because ACA interacts with N217 and K410 that lie outside the YxxØ-binding cavity formed by residues F174, D176, K203, and R423 (*26*), an allosteric activation mechanism of AP2 may exist (Fig. 4E). Besides AP subunit genes (AP1M1, AP2A1, AP2M1, and AP3S2), several syntaxin-relevant genes (STX5, STX10, and STXBP2) were identified to play a proviral role (Fig. 1B and fig. S1). Four pharmacological inhibitors including imperatorin, Pyr6, ZD7288, and ethosuximide exhibited potent anti-influenza activity with an EC_{99} at nanomolar range (Fig. 1C). Further characterization of their underlying mechanisms is warranted.

Establishment of the CWID platform enables identification of drug-binding target(s) in an unbiased manner, which addresses a common difficulty that challenges all phenotypic forward chemical screening (Fig. 4, C and D). This platform may be adopted for studies using host-targeting strategies to accelerate the progress of drug target discovery. Overall, we demonstrate that the AP2M1/YxxØ interaction is a druggable target for broad-spectrum antiviral therapy, and virus YxxØ mutant could be tested as attenuated vaccines. These approaches may provide additive and possibly synergistic antiviral effects when ACA or its analogs are combined with other antiviral agents for tackling emerging viral infections.

MATERIALS AND METHODS

Experimental design

The main goal of this study was to identify a next generation of broad-spectrum antiviral with elucidated machinery. First, we comprehensively evaluated the antiviral potency of the selected drug ACA in cell cultures, ex vivo and in vivo models. Second, we established an integrative platform, named CWID, to identify the host AP2M1/YxxØ interaction as the ACA drug target and in an unbiased manner. Third, we investigated the biological importance of AP2M1/YxxØ interaction in the viral replication cycle using three representative viruses. Last, we characterized the effect of virulence of the substitutions in influenza A NP YxxØ motif.

Cells and viruses

HBTECs were cultured with airway epithelial cell basal medium according to the manufacturer's protocol. Human-induced pluripotent stem cell–derived neural progenitor cells (NPCs) were cultured and differentiated according to a previous protocol (*27*). Human lung fibroblast HFL1 was cultured in F-12K medium. Human T lymphoblast MOLT-4 $CCR5^+$ cells were cultured in RPMI 1640 medium supplemented with 10% heat-inactivated fetal bovine serum (FBS) and G418 (1 mg/ml). Human embryonic kidney (HEK) 293T cells, human lung carcinoma (A549) cells, human hepatoma (Huh7) cells, human RD cells, human epithelial type 2 cells, MDCK cells, and African green monkey kidney (Vero) cells were maintained in Dulbecco's modified Eagle's medium (DMEM) medium. All culture medium was supplemented with 10% heat-inactivated FBS, penicillin (50 U/ml), and streptomycin (50 μg/ml). All cells were confirmed to be free of mycoplasma contamination by the Plasmo Test (InvivoGen). The IAV strains A/Hong Kong/415742/2009(H1N1)pdm09, A/Anhui/1/2013(H7N9), A/Vietnam/1194/2004(H5N1), A/Netherlands/219/2003(H7N7), and A/HK/1073/1999 (H9N2) were cultured in embryonated chicken eggs. The SARS-CoV-2 HKU-001a was isolated from the nasopharyngeal aspirate specimen of a laboratory-confirmed COVID-19 patient in Hong Kong (*28*). The MERS-CoV (HCoV-EMC/2012, a gift from R. Fouchier) and SARS-CoV (GZ50) were propagated in Vero-E6 cells. The HIV-1 JR-FL virus (#4984, National Institutes of Health AIDS) was propagated in MOLT-4 $CCR5^+$ cells in the presence of interleukin-2 (1 ng/ml) for 14 days as we previously described (*29*). Enterovirus A-71 (SZ/HK08-5) was cultured in RD cells. The ZIKV (Puerto Rico strain PRVABC59, a gift from B. Russell and B. Johnson, CDC, USA) was amplified in Vero cells. A clinical isolate of human AdV5 was propagated in A549 cells. The SFTSV HB29 strain (a gift from M. Liang, CDC, China) was propagated in Vero cells. All cultured viruses were titrated by PFU assays and/or 50% tissue culture infectious dose ($TCID_{50}$) assay and/or quantitative reverse transcription polymerase chain reaction (RT-qPCR) assays and/or p24 ELISA as indicated. All virus stocks were kept at −80°C in aliquots. All experiments with live viruses were conducted using biosafety level 2 or 3 facility as we previously described (*30*).

Plasmids, primers, and biological reagents

Wnt signaling reporter containing T cell factor/lymphoid enhancer–binding factor was a gift from R. Moon (Addgene plasmid #12456). TGF-β signaling reporter containing four copies of the Smad binding site was shared by B. Vogelstein (Addgene plasmid #16495). Notch signaling reporter containing centromere-binding protein 1 (CBF1)–responsive element was obtained from N. Gaiano (Addgene plasmid #26897). PI3K/Akt signaling reporter containing forkhead-responsive element was a gift from M. Greenberg (Addgene plasmid #1789). All primer sequences used are provided in table S2. ACA was purchased from Cayman Chemical (Michigan, USA). Other chemical inhibitors were obtained from Sigma-Aldrich (Missouri, USA) unless specified. All peptides were synthesized from Cellmano Biotech (Hefei, China) with >95% purity. The phosphine-activated fluorescent dye DyLight 488–Phosphine (Invitrogen) was used for specific labeling and detection of azido-tagged molecules, i.e., azido-ACA. The 4′,6-diamidino-2-phenylindole (DAPI; Sigma-Aldrich), calnexin polyclonal Ab (Abbkine, ABP0065), and Phalloidin–Atto 647N (Sigma-Aldrich) were used for nuclear, ER, and cell membrane staining, respectively. Primary antibodies against human AP2M1 (Abcam, ab75995), anti–β-actin (Abcam, ab8227), anti–influenza NP (Abcam, ab104870), anti–ZIKV NS3 (GeneTex, GTX133309), anti–EV-A71 2C (GeneTex, GTX132354), anti–His-tag (Invitrogen, MA1-21315), anti–HA-tag (Abbkine, A02040), anti–Flag-tag (Sigma-Aldrich, F3165), anti–Lamin A (Abcam, ab26300), anti–glyceraldehyde-3-phosphate dehydrogenase (GAPDH; Abcam, ab8245), and anti–MERS-CoV NP mouse serum (in house) were used in relevant experiments. Alexa Fluor 488 goat anti-mouse immunoglobulin G (H + L) antibody (1:500; Invitrogen, A28175) and Alexa Fluor 594 goat-rabbit (1:500; Invitrogen, A27016) were used as secondary antibodies for immunofluorescence staining. Individual SMARTpool siRNA targeting AP2M1, TRPM2, TRPM8, or PLA2G2A was purchased from Dharmacon (Lafayette, USA). NE-PER nuclear and cytoplasmic extraction reagents (Thermo Fisher Scientific) was used according

to the manufacturer's protocol. An AP2M1 human gene knockout kit (OriGene, KN401377) was used to establish the CRISPR knockout cell lines according to the manufacturer's protocol. Immunofluorescence RNA was visualized using the ViewRNA cell plus assay kit (Invitrogen, 88-19000) containing a viewRNA type 1 probe set designed against the negative stranded RNA NP genome (vRNA) of influenza A H1N1 PR8 virus (Invitrogen, VF1-10583).

Loss-of-function screen

To identify host genes essential for H1N1pdm replication, an RNA interference (RNAi)–based screen was performed using a commercially available library targeting 142 cellular membrane–trafficking genes (Ambion Silencer, A30138). Briefly, 1.5×10^4 per well of A549 cells were seeded in 96-well plates overnight, followed by siRNA transfection once daily for two consecutive days using the Lipofectamine RNAiMAX reagent. At 48 hours after primary siRNA transfection, A549 cells were infected with 0.1 MOI virus. One hour later, the infectious inoculum was aspirated and replaced with fresh DMEM medium containing 2% BSA and N-tosyl-L-phenylalanine chloromethyl ketone (TPCK)–treated trypsin (2 μg/ml). The cell culture supernatant of individual well was collected after another 48 hours for viral load titrated by the RT-qPCR method. Before virus infection, wells exhibited poor cell viability (<80%) after gene silencing were excluded.

Chemical library screen

A small-molecule compound library with 420 candidates (MedChemExpress), targeting membrane transporters and ion channels, was used for pharmacological screening with antiviral activity. The primary screening of pdmH1N1 inhibitors was CPE inhibition based as we previously established (*30*). Viability of MDCK cells after 0.01 MOI virus infection and compound treatment (10 μM) were determined at 48 hpi using the CellTiter-Glo luminescent cell viability kit (Promega). Secondary screening was performed with viral load reduction assay. Briefly, the cell culture supernatant at 24 hpi and compound treatment (10 and 1 μM, respectively) were collected and applied for viral copy quantification by RT-qPCR methods. Favipiravir (50 μg/ml) was used as a positive control throughout the screening process.

Click chemistry/WaterLOGSY/protein ID

The CWID platform was established for identification of ACA-binding target. First, an azido-tagged ACA was chemically synthesized, (E)-4-azido-2-(3-(4-pentylphenyl)-acrylamido)benzoic acid, for the purpose of intracellular visualization via click chemistry. The azido group is reactive to the fluorescent dye DyLight 488–Phosphine, which makes it visible under a fluorescent microscope. Details of the synthetic scheme are provided in the Supplementary Materials.

WaterLOGSY, a ligand-observed NMR technique, was used to screen for ACA-interactive cellular fractions (*31*). To fractionate the pdmH1N1-infected cell lysate, 1 ml of MDCK cells (10^7 cells, 1 MOI, 6 hpi) was ultrasonicated three times for 10 s on ice and then centrifuged. The clarified supernatant was applied for fast protein liquid chromatography (ÄKTAexplorer, GE Healthcare) using the 320-ml HiLoad 26/600 Superdex 200 preparative size exclusion chromatography column to harvest each protein fraction with ultraviolet 260-nm signals. ACA WaterLOGSY experiments were conducted on a 600-MHz Bruker Avance spectrometer using a 5-mm PASEI probe. The pulse scheme used for WaterLOGSY experiment was "ephogsygpno.2" with water suppression using excitation sculpting with gradients (*32*). All experiments were conducted at 298 K using 5-mm-diameter NMR tubes with a sample volume of 500 μl and 17 μM ACA supplemented and recorded using 4 K scans. All samples were dissolved in 95% H_2O and 5% D_2O with final concentration of 70 μM trimethylsilylpropanoic acid as internal standard. Control spectrum was recorded under the same conditions without cellular fraction to confirm the absence of self-aggregated ACA macromolecules.

To identify the ACA-binding protein target (protein IDs), the cellular fraction was lyophilized before resuspended with 10 μl of H_2O and incubated with 70 μM azido-ACA for 1 hour. The mixtures were further incubated with 100 μM DyLight 488–Phosphine for 3 hours to allow linkage of fluorescent dye with the azido group, before loading to a 10% nondenaturing native gel for electrophoresis. Subsequently, a Typhoon FLA 9500 laser scanner using AlexaFluor 488 filter was used to visualize the fluorescent bands that were associated with azido-ACA other than ACA. The photomultiplier tube voltage was set as 300 to 350 V and the resolution as 50 μm. Target bands were excised and subjected to LC-electrospray ionization MS/MS analysis by Q Exactive as previously established (Shanghai Applied Protein Technology Co. Ltd.) (*33*). Samples with or without ACA were also incubated with DyLight 488–Phosphine to act as controls.

Gain-of-function validation

To validate the target protein essential for ACA-dependent mode of action, eight protein IDs as revealed by the CWID platform were overexpressed individually and screened for their capacity to antagonize the ACA's antiviral activity. ORF clone of each protein was obtained from Mission TRC3 human ORF collection (Merck). In a 24-well plate, MDCK cells were transfected with 500 ng of each plasmid and incubated for 48 hours before pdmH1N1 infection. Cell culture supernatants of the infected cells, with or without ACA (5 μM), were collected for viral titer determination by standard plaque assay.

Virus infection in human AOs

Under the protocol approved by the Institutional Review Board (UW 13-364) of University of Hong Kong/Hospital Authority Hong Kong West Cluster, normal human lung tissue from a patient was obtained surgically. Informed consent was obtained from the human participant, and the experiments were performed in compliance with the approved standard operating procedures. Anti–influenza activity of ACA was also evaluated in 3D human AOs, as we previously reported (*14*). Briefly, the 3D AOs were sheared mechanically to expose the apical surface to the virus inoculum. The sheared organoids were then incubated with viruses at a MOI of 0.01 for 2 hours at 37°C. After washing, the inoculated organoids were re-embedded in Matrigel and cultured in the medium containing ACA (10 μM) or DMSO (0.1%). At the indicated times, AOs were harvested for the quantification of intracellular viral load or fixed for immunofluorescence staining.

Mouse experiments

BALB/c mice, hDPP4 transgenic C57BL/6 mice, and interferon receptor α/β knockout ($IFNAR^{-/-}$) A129 mice were kept in biosafety level 2 or 3 housing and given access to standard pellet feed and water ad libitum, as we previously described (*34*–*36*). All experimental protocols were approved by the Animal Ethics Committee (CULATAR 4057-16, 4371-17, 4511-17) in the University of Hong Kong and were

performed according to the standard operating procedures of the biosafety level 2 or 3 animal facilities. To evaluate the cross-subtype anti–influenza virus efficacy of ACA in vivo, BALB/c mice (20 mice per group) were inoculated intranasally with 200 PFU of influenza A H7N9 virus or 1000 PFU of mouse-adapted influenza A H1N1 virus in 20-μl PBS. Treatment was performed 1 hour after challenge by intranasal administration. One group of mice was inoculated with 20 μl of ACA (0.2 mg/kg). A second group was treated with 20 μl of intranasal zanamivir (2 mg/kg) (*30*). A third group was given intranasally 0.5% DMSO in PBS as an untreated control. Animal survival and clinical disease were monitored for 14 days or until death. Lung tissues (five mice per group) were collected for viral load detection and hematoxylin and eosin (H&E) histopathologic analyses on days 2 and 4 after challenge, respectively.

To evaluate the anti-ZIKV efficacy of ACA in vivo, 4- to 6-week-old A129 mice were randomly divided into two groups to receive ACA treatment or sham treatment through the subcutaneous route (n = 13 per group). The mice were inoculated subcutaneously with 1×10^6 PFU (in 100-μl PBS) of ZIKV-PR under anesthesia. Each mouse was then received one dose of subcutaneous-administered ACA (1 mg/kg) or 0.5% DMSO in PBS at 1 hpi. The mice were monitored daily for body weight change and clinical signs of disease. Five mice in each group were euthanized at 6 dpi, and brain tissues were harvested for vial titers and histopathologic and immunohistochemistry analyses. The survival of the other mice was monitored until 14 dpi.

To examine the anti–MERS-CoV activity of ACA, a total of 26 mice (n = 13 per group) were evaluated. After anesthesia, mice were intranasally inoculated with 20 μl of virus suspension containing 500 PFU of MERS-CoV. Intranasal therapeutic treatments were initiated at 1 hpi. One group of mice was inoculated with 20 μl of ACA (0.2 mg/kg). The other group was given intranasally 0.5% DMSO in PBS as an untreated control. Animal survival and clinical disease were monitored for 14 days or until death. Five mice in each group were euthanized randomly on 2 dpi, respectively. Mouse lungs were collected for virus titration and H&E histopathologic and immunofluorescence staining.

Ex vivo imaging

The whole-organ lungs and brains of the GFP virus–infected mice were excised at the indicated time after challenge. After fixation in 4% paraformaldehyde for overnight, the images were acquired in a PE IVIS Spectrum in vivo imaging system fitted with GFP excitation/emission filters.

Live cell imaging

Live imaging was used to visualize the cotrafficking of AP2M1 and influenza A NP according to a previous report with some modifications (*37*). Time-lapse images were taken using the Nikon Ti2-E Widefield Microscope with a 100× 1.46 oil objective in a heated (37°C) chamber. GFP-labeled NP protein and mCherry-fused AP2M1 protein were tracked by sequential imaging every 2 s with 50- and 200-ms exposures for each channel, respectively. Individual colocalized puncta run lengths and transport velocities were calculated using the Track Points for MetaMorph analysis software, measuring the distance traveled (in any direction) between frames for each respective puncta. The movies were made using the Stack function for MetaMorph analysis software via accumulating the relative frames in order.

Reverse genetics

The recombinant influenza virus carrying a GFP reporter gene in the NS segment (NS1-GFP virus) was rescued using standard reverse genetics techniques (*38*). The 8-plasmid system, with A/duck/Hubei/WH18/2015(H5N6) background, was a gift from J. Meilin (Huazhong Agricultural University, China). NP constructs harboring YxxØ mutations, i.e., pHWNP-Y296A, pHWNP-V299A, pHWNP-V299L, pHWNP-Y385A, pHWNP-I388A, and pHWNP-I388L, were performed by site-directed mutagenesis (Stratagene) based on the WT pHWNP plasmid. Titers of viral stocks were determined by plaque assay on MDCK cells.

Reporter gene assays

Luciferase reporter plasmids reflecting the up- or down-regulation of cell fate determination pathways were used. Experimentally, individual reporter plasmid (100 ng), together with a transfection efficiency control plasmid (pNL1.1.TK, Promega) construct (5 ng), was cotransfected into the indicated cells for 24 hours. Subsequently, 10 MOI of each virus was used to infect the transfected cells, followed by luminance detection at 0, 1, 3, 6, or 12 hpi according to the manufacturer's protocol (dual-luciferase reporter assay system, Promega). The transfected cell with mock infection was taken as a baseline control for normalization. Influenza A virus mini-genome reporter assays were performed as described previously with some modifications (*39*). RNP complexes composed of PA, PB1, PB2, and NP or their mutants were mixed with a luciferase reporter plasmid (50 ng each) and pNL1.1.TK construct (5 ng) and then cotransfected into HEK293T cells. Luminescence was determined at 24 hours after transfection.

YxxØ motif binding assay

The assay was designed to detect AP2M1 and YxxØ binding. Free or biotin-labeled YxxØ motif, with a peptide sequence of DYQRLN, was synthesized. To expose the AP2M1 binding site, Calyculin A, an inhibitor of AP2M1 dephosphorylation which "locks" AP2M1 in its YxxØ binding active conformation, was added according to a previous report (*24*). HEK293T cells in six-well plates were transfected with His-AP2M1 or its low binding affinity mutant D176A for 48 hours. Next, 10 μg per well transfected cell lysate containing the overexpressed proteins was incubated with the Ni-NTA HisSorb 96-well plate (Qiagen) for overnight at 4°C. After washing, drugs were added 1 hour before incubation, followed by input of Biotin-YxxØ probe (10 μg/ml) and detection of binding signal using horseradish peroxidase–conjugated streptavidin (Thermo Fisher Scientific, N100) and trimethylboron substrate (Thermo Fisher Scientific, N301). In this experiment, the unlabeled peptide DYQRLN was used as a positive control binding inhibitor, while mock-transfected cell lysate was taken as a background control. The washing and dilution buffer consisting 100 nM Calyculin A, PBS, and 0.1% Tween-20 was used throughout the assay.

Molecular docking analysis

The ACA (PubChem CID: 5353376) 3D structure was downloaded from PubChem database. LeadFinder version 1804 was used to perform ligand-receptor docking (*40*). Extra precision mode (-xp) was applied to search the ligand conformational space more thoroughly. Energy grid map was generated according to the binding pose of YxxØ motif in the AP2M1/YxxØ complex structure (Protein Data Bank code: 2XA7) (*7*). Default grid map spacing of 0.375A was set

for a good trade-off between accuracy and performance. Bond orders were assigned, hydrogens were added, and cap termini were included with the Protein Preparation Wizard module as implemented in Maestro. Protonation states of side chains were predicted using PROPKA3.1 server. Partial charges over all atoms were assigned within the AMBER99 force field scheme as implemented in AmberTools. The top-ranked pose was visualized by using PyMOL, while 2D intermolecular interaction was visualized with LigPlot+.

Statistical analysis

Data were analyzed using GraphPad Prism 7 (GraphPad Software, San Diego, CA, USA). The values shown in the graphs are presented as means ± SD of at least three independent experiments. Statistical differences between groups were analyzed using a one-way analysis of variance (ANOVA) statistical test with Dunnett's multiple comparisons tests or two-tailed unpaired *t* tests. Colocalization rate was quantified using ImageJ (JACoP) colocalization software and Manders' colocalization coefficients (MCCs) as previously described (*23*). $P < 0.05$ was considered statistically significant.

SUPPLEMENTARY MATERIALS

Supplementary material for this article is available at http://advances.sciencemag.org/cgi/content/full/sciadv.aba7910/DC1

View/request a protocol for this paper from *Bio-protocol*.

REFERENCES AND NOTES

1. N. K. Duggal, M. Emerman, Evolutionary conflicts between viruses and restriction factors shape immunity. *Nat. Rev. Immunol.* **12**, 687–695 (2012).
2. J. F. W. Chan, S. K. P. Lau, K. K. W. To, V. C. C. Cheng, P. C. Y. Woo, K.-Y. Yuen, Middle East respiratory syndrome coronavirus: Another zoonotic betacoronavirus causing SARS-like disease. *Clin. Microbiol. Rev.* **28**, 465–522 (2015).
3. D. Musso, D. J. Gubler, Zika virus. *Clin. Microbiol. Rev.* **29**, 487–524 (2016).
4. K. K. W. To, J. F. W. Chan, H. Chen, L. Li, K. Y. Yuen, The emergence of influenza A H7N9 in human beings 16 years after influenza A H5N1: A tale of two cities. *Lancet Infect. Dis.* **13**, 809–821 (2013).
5. N. Perrimon, C. Pitsouli, B.-Z. Shilo, Signaling mechanisms controlling cell fate and embryonic patterning. *Cold Spring Harb. Perspect. Biol.* **4**, a005975 (2012).
6. L. Zhu, L. Wang, X. Luo, Y. Zhang, Q. Ding, X. Jiang, X. Wang, Y. Pan, Y. Chen, Tollip, an intracellular trafficking protein, is a novel modulator of the transforming growth factor-β signaling pathway. *J. Biol. Chem.* **287**, 39653–39663 (2012).
7. L. P. Jackson, B. T. Kelly, A. J. McCoy, T. Gaffry, L. C. James, B. M. Collins, S. Höning, P. R. Evans, D. J. Owen, A large-scale conformational change couples membrane recruitment to cargo binding in the AP2 clathrin adaptor complex. *Cell* **141**, 1220–1229 (2010).
8. D. Yao, M. Ehrlich, Y. I. Henis, E. B. Leof, Transforming growth factor-β receptors interact with AP2 by direct binding to β2 subunit. *Mol. Biol. Cell* **13**, 4001–4012 (2002).
9. Z. Kadlecova, S. J. Spielman, D. Loerke, A. Mohanakrishnan, D. K. Reed, S. L. Schmid, Regulation of clathrin-mediated endocytosis by hierarchical allosteric activation of AP2. *J. Cell Biol.* **216**, 167–179 (2017).
10. I. Yakymovych, M. Yakymovych, C. H. Heldin, Intracellular trafficking of transforming growth factor β receptors. *Acta Biochim. Biophys. Sin.* **50**, 3–11 (2018).
11. X. Wen, L. Ding, E. Hunter, P. Spearman, An siRNA screen of membrane trafficking genes highlights pathways common to HIV-1 and M-PMV virus assembly and release. *PLOS ONE* **9**, e106151 (2014).
12. D. McCormick, Y.-T. Lin, F. Grey, Identification of host factors involved in human cytomegalovirus replication, assembly, and egress using a two-step small interfering RNA screen. *mBio* **9**, e00716-18 (2018).
13. A. Karlas, N. Machuy, Y. Shin, K. P. Pleissner, A. Artarini, D. Heuer, D. Becker, H. Khalil, L. A. Ogilvie, S. Hess, A. P. Mäurer, E. Müller, T. Wolff, T. Rudel, T. F. Meyer, Genome-wide RNAi screen identifies human host factors crucial for influenza virus replication. *Nature* **463**, 818–822 (2010).
14. J. Zhou, C. Li, N. Sachs, M. C. Chiu, B. H.-Y. Wong, H. Chu, V. K. M. Poon, D. Wang, X. Zhao, L. Wen, W. Song, S. Yuan, K. K. Y. Wong, J. F. W. Chan, K. K. W. To, H. Chen, H. Clevers, K. Y. Yuen, Differentiated human airway organoids to assess infectivity of emerging influenza virus. *Proc. Natl. Acad. Sci. U.S.A.* **115**, 6822–6827 (2018).
15. C. Harteneck, H. Frenzel, R. Kraft, *N*-(p-amylcinnamoyl)anthranilic acid (ACA): A phospholipase A_2 inhibitor and TRP channel blocker. *Cardiovasc. Drug Rev.* **25**, 61–75 (2007).
16. E. Bekerman, G. Neveu, A. Shulla, J. Brannan, S.-Y. Pu, S. Wang, F. Xiao, R. Barouch-Bentov, R. R. Bakken, R. Mateo, J. Govero, C. M. Nagamine, M. S. Diamond, S. de Jonghe, P. Herdewijn, J. M. Dye, G. Randall, S. Einav, Anticancer kinase inhibitors impair intracellular viral trafficking and exert broad-spectrum antiviral effects. *J. Clin. Invest.* **127**, 1338–1352 (2017).
17. T. Watanabe, E. Kawakami, J. E. Shoemaker, T. J. S. Lopes, Y. Matsuoka, Y. Tomita, H. Kozuka-Hata, T. Gorai, T. Kuwahara, E. Takeda, A. Nagata, R. Takano, M. Kiso, M. Yamashita, Y. Sakai-Tagawa, H. Katsura, N. Nonaka, H. Fujii, K. Fujii, Y. Sugita, T. Noda, H. Goto, S. Fukuyama, S. Watanabe, G. Neumann, M. Oyama, H. Kitano, Y. Kawaoka, Influenza virus-host interactome screen as a platform for antiviral drug development. *Cell Host Microbe* **16**, 795–805 (2014).
18. D. J. Owen, B. M. Collins, P. R. Evans, Adaptors for clathrin coats: Structure and function. *Annu. Rev. Cell Dev. Biol.* **20**, 153–191 (2004).
19. A. Nesterov, R. E. Carter, T. Sorkina, G. N. Gill, A. Sorkin, Inhibition of the receptor-binding function of clathrin adaptor protein AP-2 by dominant-negative mutant mu2 subunit and its effects on endocytosis. *EMBO J.* **18**, 2489–2499 (1999).
20. D. N. Banbury, J. D. Oakley, R. B. Sessions, G. Banting, Tyrphostin A23 inhibits internalization of the transferrin receptor by perturbing the interaction between tyrosine motifs and the medium chain subunit of the AP-2 adaptor complex. *J. Biol. Chem.* **278**, 12022–12028 (2003).
21. W.-F. Tang, S.-Y. Yang, B.-W. Wu, J.-R. Jheng, Y.-L. Chen, C.-H. Shih, K.-H. Lin, H.-C. Lai, P. Tang, J.-T. Horng, Reticulon 3 binds the 2C protein of enterovirus 71 and is required for viral replication. *J. Biol. Chem.* **282**, 5888–5898 (2007).
22. T. Mitsunari, F. Nakatsu, N. Shioda, P. E. Love, A. Grinberg, J. S. Bonifacino, H. Ohno, Clathrin adaptor AP-2 is essential for early embryonal development. *Mol. Cell. Biol.* **25**, 9318–9323 (2005).
23. G. Neveu, A. Ziv-Av, R. Barouch-Bentov, E. Berkerman, J. Mulholland, S. Einav, AP-2-associated protein kinase 1 and cyclin G-associated kinase regulate hepatitis C virus entry and are potential drug targets. *J. Virol.* **89**, 4387–4404 (2015).
24. G. Neveu, R. Barouch-Bentov, A. Ziv-Av, D. Gerber, Y. Jacob, S. Einav, Identification and targeting of an interaction between a tyrosine motif within hepatitis C virus core protein and AP2M1 essential for viral assembly. *PLOS Pathog.* **8**, e1002845 (2012).
25. J. R. Simard, D. Rauh, FLiK: A direct-binding assay for the identification and kinetic characterization of stabilizers of inactive kinase conformations. *Methods Enzymol.* **548**, 147–171 (2014).
26. B. M. Collins, A. J. McCoy, H. M. Kent, P. R. Evans, D. J. Owen, Molecular architecture and functional model of the endocytic AP2 complex. *Cell* **109**, 523–535 (2002).
27. S. Cai, L. Han, Q. Ao, Y. S. Chan, D. K.-Y. Shum, Human induced pluripotent cell-derived sensory neurons for fate commitment of bone marrow-derived Schwann cells: Implications for remyelination therapy. *Stem Cells Transl. Med.* **6**, 369–381 (2017).
28. H. Chu, J. F. W. Chan, Y. Wang, T. T. T. Yuen, Y. Chai, Y. Hou, H. Shuai, D. Yang, B. Hu, X. Huang, X. Zhang, J. P. Cai, J. Zhou, S. Yuan, K. H. Kok, K. K. W. To, I. H. Y. Chan, A. J. Zhang, K. Y. Sit, W. K. Au, K. Y. Yuen, Comparative replication and immune activation profiles of SARS-CoV-2 and SARS-CoV in human lungs: An ex vivo study with implications for the pathogenesis of COVID-19. *Clin. Infect. Dis.*, ciaa410 (2020).
29. K.-W. Cheung, T. Wu, S. F. Ho, Y. C. Wong, L. Liu, H. Wang, Z. Chen, $\alpha_4\beta_7^+$ $CD4^+$ effector/effector memory T cells differentiate into productively and latently infected central memory T cells by transforming growth factor β1 during HIV-1 Infection. *J. Virol.* **92**, e01510-17 (2018).
30. S. Yuan, H. Chu, J. F.-W. Chan, Z. W. Ye, L. Wen, B. Yan, P.-M. Lai, K.-M. Tee, J. Huang, D. Chen, C. Li, X. Zhao, D. Yang, M. C. Chiu, C. Yip, V. K.-M. Poon, C. C.-S. Chan, K.-H. Sze, J. Zhou, I. H.-Y. Chan, K.-H. Kok, K. K.-W. To, R. Y.-T. Kao, J. Y.-N. Lau, D.-Y. Jin, S. Perlman, K.-Y. Yuen, SREBP-dependent lipidomic reprogramming as a broad-spectrum antiviral target. *Nat. Commun.* **10**, 120 (2019).
31. K.-H. Sze, W.-H. Lam, H. Zhang, Y.-H. Ke, M.-K. Tse, P. C. Y. Woo, S. K. P. Lau, C. C. Y. Lau, J.-P. Cai, E. T. K. Tung, R. K. C. Lo, S. Xu, R. Y. T. Kao, Q. Hao, K.-Y. Yuen, Talaromyces marneffei Mp1p Is a Virulence Factor that Binds and Sequesters a Key Proinflammatory Lipid to Dampen Host Innate Immune Response. *Cell Chem. Biol.* **24**, 182–194 (2017).
32. H. Tse, Q. Gu, K.-H. Sze, I. K. Chu, R. Y.-T. Kao, K.-C. Lee, C.-W. Lam, D. Yang, S. S.-C. Tai, Y. Ke, E. Chan, W.-M. Chan, J. Dai, S.-P. Leung, S.-Y. Leung, K.-Y. Yuen, A tricyclic pyrrolobenzodiazepine produced by *Klebsiella oxytoca* is associated with cytotoxicity in antibiotic-associated hemorrhagic colitis. *J. Biol. Chem.* **292**, 19503–19520 (2017).
33. X. Ding, J. Xu, C. Wang, Q. Feng, Q. Wang, Y. Yang, H. Lu, F. Wang, K. Zhu, W. Li, Q. Yan, S.-J. Gao, C. Lu, Suppression of the SAP18/HDAC1 complex by targeting TRIM56

and Nanog is essential for oncogenic viral FLICE-inhibitory protein-induced acetylation of p65/RelA, NF-κB activation, and promotion of cell invasion and angiogenesis. *Cell Death Differ.* **26**, 1970–1986 (2019).
34. J. Zhou, C. Li, G. Zhao, H. Chu, D. Wang, H. H.-N. Yan, V. K.-M. Poon, L. Wen, B. H.-Y. Wong, X. Zhao, M. C. Chiu, D. Yang, Y. Wang, R. K. H. Au-Yeung, I. H.-Y. Chan, S. Sun, J. F.-W. Chan, K. K.-W. To, Z. A. Memish, V. M. Corman, C. Drosten, I. F.-N. Hung, Y. Zhou, S. Y. Leung, K.-Y. Yuen, Human intestinal tract serves as an alternative infection route for Middle East respiratory syndrome coronavirus. *Sci. Adv.* **3**, eaao4966 (2017).
35. B. J. Zheng, K. W. Chan, Y. P. Lin, G. Y. Zhao, C. Chan, H. J. Zhang, H. L. Chen, S. S. Y. Wong, S. K. P. Lau, P. C. Y. Woo, K. H. Chan, D. Y. Jin, K. Y. Yuen, Delayed antiviral plus immunomodulator treatment still reduces mortality in mice infected by high inoculum of influenza A/H5N1 virus. *Proc. Natl. Acad. Sci. U.S.A.* **105**, 8091–8096 (2008).
36. J. F. Chan, Z. Zhu, H. Chu, S. Yuan, K. K.-H. Chik, C. C.-S. Chan, V. K.-M. Poon, C. C.-Y. Yip, X. Zhang, J. O.-L. Tsang, Z. Zou, K.-M. Tee, H. Shuai, G. Lu, K.-Y. Yuen, The celecoxib derivative kinase inhibitor AR-12 (OSU-03012) inhibits Zika virus via down-regulation of the PI3K/Akt pathway and protects Zika virus-infected A129 mice: A host-targeting treatment strategy. *Antiviral Res.* **160**, 38–47 (2018).
37. K. E. Coller, N. S. Heaton, K. L. Berger, J. D. Cooper, J. L. Saunders, G. Randall, Molecular determinants and dynamics of hepatitis C virus secretion. *PLOS Pathog.* **8**, e1002466 (2012).
38. J. T. Perez, A. Garcia-Sastre, B. Manicassamy, Insertion of a GFP reporter gene in influenza virus. *Curr. Protoc. Microbiol.* **29**, 15.G.4.1–15.G.4.16 (2013).
39. W. Song, P. Wang, B. W.-Y. Mok, S.-Y. Lau, X. Huang, W.-L. Wu, M. Zheng, X. Wen, S. Yang, Y. Chen, L. Li, K.-Y. Yuen, H. Chen, The K526R substitution in viral protein PB2 enhances the effects of E627K on influenza virus replication. *Nat. Commun.* **5**, 5509 (2014).
40. O. V. Stroganov, F. N. Novikov, V. S. Stroylov, V. Kulkov, G. G. Chilov, Lead finder: An approach to improve accuracy of protein–ligand docking, binding energy estimation, and virtual screening. *J. Chem. Inf. Model.* **48**, 2371–2385 (2008).

Acknowledgments: We would like to thank the technical support provided by the Core Facility of the LKS Faculty of Medicine, The University of Hong Kong. **Funding:** This work was partly supported by the donations of Michael Seak-Kan Tong, the Shaw Foundation Hong Kong, Richard Yu and Carol Yu, Respiratory Viral Research Foundation Limited, May Tam Mak Mei Yin, Hui Ming, Hui Hoy and Chow Sin Lan Charity Fund Limited, Chan Yin Chuen Memorial Charitable Foundation, Marina Man-Wai Lee, the Hong Kong Hainan Commercial Association South China Microbiology Research Fund, the Jessie & George Ho Charitable Foundation, and Perfect Shape Medical; and funding from the Theme-based Research Scheme (T11-707/15-R) of the Research Grants Council, Hong Kong Special Administrative Region; and the High Level-Hospital Program, Health Commission of Guangdong Province, China. The sponsors had no role in the design and conduct of the study, in the collection, analysis, and interpretation of data, or in the preparation, review, or approval of the manuscript. **Author contributions:** S.Y., J.F.-W.C., and K.-Y.Y. designed the study. S.Y., H.C., J.H., Z.-W.Y., Y.M., J.-P.C., R.L., and J.C. performed experiments and collected data. L.W. performed the molecular docking. P.-M.L. and K.-H.S. performed WaterLOGSY. S.Y. and J.F.W.-C. provided the animal experimental data. J.Z. and X.Z. provided the organoid data. V.K.-M.P. contributed to the histopathologic examination. K.K.W.-T., Z.C., H.C., and D.-Y.J. gave conceptual advice and discussion. J.F.-W.C. and K.-Y.Y. supervised the study. S.Y., J.F.-W.C., and K.Y.Y. wrote the manuscript. All authors read and approved the final manuscript. **Competing interests:** S.Y., J.F.-W.C. and K.-Y.Y. are authors on a provisional patent application related to this work filed by Avalon Flaviviral Therapeutics (HK) Limited (no. 63/024266; filed 13 May 2020). The authors declare that they have no other competing interests. **Data and materials availability:** All data needed to evaluate the conclusions in the paper are present in the paper and/or the Supplementary Materials. Additional data including supplementary data sheet and chemical synthesis scheme are available in Dryad repository with a DOI (doi:10.5061/dryad.4qrfj6q79) for access and/or may be requested from the authors.

Submitted 6 January 2020
Accepted 14 July 2020
Published First Release 14 August 2020
Published 28 August 2020
10.1126/sciadv.aba7910

Citation: S. Yuan, H. Chu, J. Huang, X. Zhao, Z.-W. Ye, P.-M. Lai, L. Wen, J.-P. Cai, Y. Mo, J. Cao, R. Liang, V. K.-M. Poon, K.-H. Sze, J. Zhou, K. K.-W. To, Z. Chen, H. Chen, D.-Y. Jin, J. F.-W. Chan, K.-Y. Yuen, Viruses harness YxxØ motif to interact with host AP2M1 for replication: A vulnerable broad-spectrum antiviral target. *Sci. Adv.* **6**, eaba7910 (2020).